ISTANBUL TECHNICAL UNIVERSITY ★ GRADUATE SCHOOL OF SCIENCE ENGINEERING AND TECHNOLOGY

NUMERICAL MODELLING AND SIMULATION OF A SQUEEZE FILM DAMPER

M.Sc. THESIS

Ekin AKBULUT

Department of Mechanical Engineering

Automotive Engineering Programme

JULY 2020

ISTANBUL TECHNICAL UNIVERSITY ★ GRADUATE SCHOOL OF SCIENCE ENGINEERING AND TECHNOLOGY

NUMERICAL MODELLING AND SIMULATION OF A SQUEEZE FILM DAMPER

M.Sc. THESIS

Ekin AKBULUT
(503161719)

Department of Mechanical Engineering

Automotive Engineering Programme

Thesis Advisor: Prof. Dr. Özgen AKALIN

JULY 2020

ISTANBUL TEKNİK ÜNİVERSİTESİ ★ FEN BİLİMLERİ ENSTİTÜSÜ

SIKIŞTIRMA ETKİLİ YAĞ FİLM SÖNÜMLEYİCİNİN SAYISAL MODELLENMESİ VE SİMÜLASYONLARI

YÜKSEK LİSANS TEZİ

Ekin AKBULUT
(503161719)

Makine Mühendisliği Anabilim Dalı

Otomotiv Mühendisliği Programı

Tez Danışmanı: Prof. Dr. Özgen AKALIN

TEMMUZ 2020

Ekin Akbulut, a M.Sc. student of İTU Graduate School of Science Engineering and Technology student ID 503161719, successfully defended the thesis/dissertation entitled "NUMERICAL MODELLING AND SIMULATION OF A SQUEEZE FILM DAMPER", which she prepared after fulfilling the requirements specified in the associated legislations, before the jury whose signatures are below.

Thesis Advisor :	**Prof. Dr. Özgen AKALIN** İstanbul Technical University	....
Jury Members :	**Assis. Prof. Dr. Osman Taha Şen** İstanbul Technical University	....
	Prof. Dr. Muammer Özkan Yıldız Technical University	....

Date of Submission : 15 June 2020
Date of Defense : 7 July 2020

To my dear family,

FOREWORD

I would like to express my sincere gratitude and thank to Prof. Dr. Özgen Akalın for his kind support and supervision to perform and complete my Master's study. Without his advices and encouragement throughout this study, I would not have been able to achieve this accomplishment. It was amazing to have such a supportive supervisor who was always ready to help.

My greatest thanks to my mother and sister, Hürriyet Akbulut and Özge Akbulut, for their lifetime support with all my decisions. I could not complete this step of my life without their help.

June 2020

Ekin AKBULUT
(Mechanical Engineer)

TABLE OF CONTENTS

Page

ABBREVIATIONS

SFD **:** Squeeze Film Damper

SOR **:** Successive Over-Relaxation

LIST OF SYMBOLS

c	: Bearing radial clearance [m]
D	: Shaft diameter [m]
e	: Eccentricity [m]
$\mathbf{e_x}$	: Eccentricity in horizontal axis [m]
$\mathbf{e_y}$	: Eccentricity in vertical axis [m]
$\mathbf{F_r}$	: Reaction force along radial direction
$\mathbf{F_t}$	: Reaction force along tangential direction
h	: Oil film thickness [m]
$\mathbf{h_{max}}$	: Maximum oil film thickness [m]
$\mathbf{h_{min}}$	: Minimum oil film thickness [m]
H	: Dimensionless oil film thickness
L	: Bearing length [m]
M	: Number of elements along circumferential direction
N	: Number of elements along axial direction
p	: Pressure [Pa]
P	: Dimensionless pressure
$\mathbf{P_{new}}$	: Dimensionless calculated new pressure
$\mathbf{P_{old}}$	: Dimensionless calculated old pressure
r	: Shaft radius [m]
Re	: Reynolds number
t	: Time [sec]
T	: Dimensionless time
$\mathbf{W_x}$	: Load along x-direction [N]
$\mathbf{W_y}$	: Load along y-direction [N]
z	: Axial coordinate
$\boldsymbol{\varepsilon}$	: Eccentricity ratio
$\boldsymbol{\varepsilon_x}$	: Eccentricity ratio in x-direction
$\boldsymbol{\varepsilon_y}$	: Eccentricity ratio in y-direction
$\boldsymbol{\theta}$	: Circumferential coordinate [rad]
$\boldsymbol{\Phi}$	: Attitude angle [rad]

ω	**:** Whirling speed [rad/sec]
w	**:** Successive over-relaxation factor
μ	**:** Oil viscosity [Pa.sec]
ρ	**:** Oil density [kg/m^3]
ΔZ	**:** Element size in axial direction
Δθ	**:** Element size in circumferential direction
λ	**:** Dimensionless bearing radius to length ratio

LIST OF TABLES

Page

LIST OF FIGURES

Page

NUMERICAL MODELLING AND SIMULATION OF A SQUEEZE FILM DAMPER

SUMMARY

The squeeze film damper is known as a type of hydrodynamic journal bearings which are used in different machines and industries such as automotive turbochargers, aircraft engines, gas turbines and compressors. It is used to improve rotordynamic response of a machine and ensures a stable operation. It also can be used to reduce vibrations due to unbalance of rotor and to reduce the loads transmitted to structural component. A typical squeeze film damper has a stationary housing and a journal which is prevented from rotation. The stationary and rotating components are separated by a film lubricant. The journal center performs an orbital motion around housing axis and this motion causes oil movement. The journal squeezes oil out from the journal surfaces and this squeeze action generates oil film pressure and provides useful cushioning. The objective of this thesis is to develop a numerical model by using MATLAB for a squeeze film damper based on Reynolds equation including fluid inertia. Oil film pressure and circular shaft orbit is simulated by using this model. Sensitivity analyses are completed to simulate the effect of different oil properties, operating conditions, and damper geometry. It is aimed that this model would serve as a basis for an evolving program that can be used in the development of future squeeze film dampers. The analytical model is validated with the experimental data found in literature. The analytical model results showed a good agreement with experimental data in terms of pressure values and behavior of the system. The oil film pressure distribution and oil film thickness along the circumference of the SFD are calculated and plotted. The maximum oil film pressure occurs at closest to the minimum film thickness location. Rotor unbalance load is strictly dependent on whirling speed. Therefore, once speed increased, unbalance load also increased. Increased unbalance load resulted with higher oil film pressures since oil is squeezed more between journal and housing surface and it created more reaction force. Final journal orbit became circular once it reaches to steady-state condition for different analyzed speeds. Due to rotor weight, the shaft orbit centers are not aligned with geometric center of housing. For higher speeds, orbit center is found closer to geometric center. Since smaller Reynolds numbers are analyzed, the significant effect of fluid inertia has not been observed. Rotor weight increase provided more oil film pressure due to oil is squeezed more. Simple central groove is modeled to divide the damper geometry into two identical segments. Peak pressures are occurred at each side of damper. Pressure decreased at groove location and this pressure decrease caused that system reached to balance condition at higher eccentricities. Groove is added to the system which journal is whirling at fixed eccentricity. In this system, pressure decrease due to groove is seen more clearly.

SIKIŞTIRMA ETKİLİ YAĞ FİLM SÖNÜMLEYİCİNİN SAYISAL MODELLENMESİ VE SİMÜLASYONLARI

ÖZET

Sıkıştırılmış yağ damperi hidrodinamik mil yatağının bir türüdür ve farklı endüstrilerde ve makine tiplerinde kullanılır. Otomotiv aşırı doldurmalarında, uçak motorlarında, gaz türbinlerinde ve kompressörlerinde kullanılır. Makinelerin rotor dinamiğini geliştirerek dengeli bir operasyon sağlar. Rotorun dengelenmemiş yükünden kaynaklanan titreşimleri ve mili destekleyen statik parçaya iletilen yükleri azaltır. Sistem genel olarak bir milden ve mili destekleyen statik bir parçadan oluşur ve bu iki parça arasında yağ bulunur. Kaymalı yataklarda olduğu gibi mil dönme hareketi yapmaz. Milin veya milin üzeride konulmuş rulmanın dış bileziğinin dönmesi dönmeyi engelleyen mekanizmalar sayesinde engellenir. Mil dönmek yerine bir yörünge etrafında titreme hareketi yapar ve bu hareket sırasında aradaki yağ belli yerlerde mil tarafından sıkıştırılır. Bu sıkıştırma hareketi mil etrafında yağ basıncı oluşturur ve statik parçaya iletilen yüklerde sönümleme veya azaltma etkisi yapar. Sıkıştırma hareketinden dolayı oluşan basınç farklı değişkenlere bağlıdır. Ana olarak yatağın ve milin geometrisine, hareket eden ve duran parça arasındaki boşluğa, yatağın uzunluğuna, milin yörünge etrafında dönme hızına, sisteme sağlanan yağın iletilme şekline, yağın özelliklerine, yağ besleme basıncına ve milin dengesizlik haline ve ağırlına bağlıdır. Oluşan yağ tabakasının kalınlığı milin yatak ekseninden yatay ve dik eksenden kaçıklığına ve milin pozisyonuna bağlıdır.

Bu tezin amacı MATLAB kullanılarak sıkıştırılmış yağ damperi için sayısal bir model oluşturmaktır. Oluşturulan modelde bazı varsayımlarda bulunuldu. Yağın vizkositesinin ve yoğunluğunun zamanla değişmediği, akışın düşük Reynolds sayılarında gerçekleştiği, yağ tabakasının ince ve yağın ağırlığının ihmal edildiği, yağın sıcaklığının sabit tutulduğu ve malzeme deformasyonun görülmediği kabul edildi. Bu kabüller ile Reynolds denklemi sadeleştirilip yağın ataleti denkleme eklendi. Sonrasında kurulan modelin doğru ve hızlı sonuç vermesi amaçlandığı için tüm denklemler boyutsuz hale getirildi. Denklemin analitik bir çözümü olmadığı için sonlu farklar yöntemi uygulanarak basit bir sayısal model elde edildi. Çözümün hızlı yakınsaması için SOR faktörü kullanılarak denklem son haline getirildi. Kurulan model ilk etapta verilen mil pozisyonu ve eksen kaçıklığı ile yağ tabakasının kalınlığını hesapladı. Sonrasında bu tabakanın kalınlığı kullanılarak yağ basıncı iteratif bir şekilde hesaplandı. Eski ve yeni hesaplanan basınç her nokta için verilen yakınsama kriterinin altına düştüğünde milin bulunduğu pozisyondaki dairesel basınç dağılımı hesaplanmış oldu. Detaylı bir kavitasyon modeli kullanılmadı. Bunun yerine yük taşıma kapasitesi kabul edilebilir bir hatayla hesaplanabilidiği için Yarı-Sommerfeld metodu kullanıldı. Bu varsayımla atmosfer basıncının altında kalan tüm basınçlar atmosfer basıncına eşitlendi. Bu çalışmada yağın oluşturduğu tepki kuvvetleri milin dengesizliğinden

doğan kuvvet ve milin ağırlığından gelen kuvvetlerle dengelendi. Kuvvet dengesi sağlanana kadar milin her açısal pozisyonu için milin eksenel kaçıklığı artırıldı. Denge sağlandığında milin bir sonraki açısal pozisyonuna geçildi. Program milin tüm açısal pozisyonları için çalıştırıldıktan sonra durduruldu.

Kurulan modelin daha sonraki sıkıştırılmış yağ damperlerinin geliştirilmesi için bir temel olması amaçlandı. Sayısal modele literatürde bulunan deneysel bir makalenin çalışma koşulları ve geometrisi girildi. Hesaplanan basınç dağılımı ve tepeden tepeye basınç değeri deneysel veri ile karşılaştırıldı. Model sonuçlarına göre oluşan basınç değerleri ve sistemin davranışı deneysel veri ile iyi bir eşleşme gösterdi. Model doğrulandıktan sonra farklı tasarım parametreleri girilerek dairesel ve eksenel olarak yağ basıncının dağılımı ve yağ tabakasının kalınlığı hesaplandı. En yüksek yağ basıncı beklenildiği gibi en düşük yağ tabakasının olduğu yerin çok yakınında gözlemlendi. Mil yağ tabakasının ince olduğu yerlerde daha fazla sıkıştırma etkisi yaptığından dolayı yüksek basınçların bu alanlara yakın yerlerde görülmesi bekleniyordu. Milin yörüngesi her açıdaki eksen kaçıklığı alınarak çizildi.

Farklı damper geometrisinin, çalışma koşullarının ve yağ özelliklerinin basınç dağılımı ve mil yörüngesi üzerindeki etkisi incelendi. Yatağın yük taşıma kapasitesi farklı durumlar için hesaplandı. İlk olarak farklı hız değerlerinin oluşan yağ basıncı üzerine etkisi incelendi. Milin dönmesinden kaynaklanan dengesiz yük milin bir yörünge etrafındaki dönme/titreme hızına fazlasıyla bağlıdır. Bundan dolayı, hız artırıldığında milin dengesizlik yükü de arrtı. Artan bu yük, yağın mil ve statik parça tarafından daha fazla sıkıştırılmasından ötürü yağ filminin basıncının artışına sebep oldu. Sistem denge durumuna geldiğinde milin dönme yörüngesi farklı hızlar için dairesel oldu. Milin ağırlığından dolayı, milin yörüngesinin merkezi statik parçanın merkezi ile eşleşmedi, yerçekimi ivmesinden ötürü yörünge merkezi yatak merkezin altında tespit edildi. Yüksek hızlarda yörüngenin merkezinin geometrik merkeze yaklaştığı gözlemlendi. Mil yatay eksenden 180 derecelik konuma geldiğinde eksenel yöndeki tepki kuvveti düşey eksende oluşan tepki kuvvetinden yüksek hızlar için daha fazla bulundu.

Küçük Reynolds sayıları analiz edildiği için yağın ataletinin oluşan yağ basıncı ve milin yörüngesinin çapında belirli bir etkisi görülmedi. Grafiklere yakından bakıldığında diğerlerine kıyasla yüksek hızda ataletin etkisi düşük hızlara göre daha fazla bulundu. Milin yörünge etrafındaki hareketinden dolayı normal şartlarda yağın sıcaklığı yapılan işle orantılı olarak artar. Sıcaklık arttığında yağın vizkozitesi düşer ve sistemin verimliliği düşer. Bu değişimi gözlemlemek için farklı viskozite değerleri için yağ basınç grafiği çizildi. Endüstride sık kullanılan ISO VG 2 yağının özellikleri kullanıldı. Beklenenin aksine düşük vizkositelerde daha fazla yağ basıncı oluştu. Kurulan modelde milin eksen kaçıklığı yük dengesini sağlamak için değiştiğinden ötürü, yağ tabakasının kalınlığı da sürekli değişti. Yağ kalınlığının tabakası sabit olmadığından ötürü farklı viskozite değerleri için basınçların karşılaştırması doğru sonuç vermedi. Model ilk başta deneysel bir makalenin verileri ile doğrulanmıştı. Bu deney düzeneğinde milin yörüngesinin yarıçapı sabit tutulduğu için yağ tabakasının kalınlığı da farklı mil pozisyonları için değişmemişti. Bu nedenle vizkositenin yağ basınç dağılımı üzerindeki etkisini doğru gözlemleyebilmek için milin yörünge yarıçapı sabit tutuldu. Düşük vizkositelerde beklenildiği gibi daha düşük basınçlar görüldü.

Milin ağırlığının etkisinin basınç dağılımı ve milin yörüngesindeki değişimini gözlemlemek için ağırlık iki katına çıkarıldı. Yağ daha fazla sıkıştırıldığından ötürü milin ağırlığının artırılması daha fazla basınç oluşmasına sebep oldu. Aynı zamanda hareket ilk başlatıldığında mil daha ağır olduğu için eksen eksen kaçıklığı daha fazla bulundu. Daha ağır mil için yük dengesinin sağlandığı durumda milin yatağın çeperlerine daha yaklaştığı gözlemlendi. Basınç dağılımının değişimine bakmak için model statik parçanın ortasına çevresel ve ölçüleri belirli olan bir oyuk konularak güncellendi. En yüksek basınç normal şartlarda ortada görülürken, oyuk yağ akışını iki eşit parçaya böldüğü için beklenildiği gibi basınç iki farklı noktada en yüksek seviyesine ulaştı. Oyuğun olduğu alanda basınç düşüklüğü yaşanmasından ötürü, sistem daha yüksek yörünge yarıçapında dengeye ulaştı. Sabit yarıçaplı yörüngeli sisteme oyuk eklendiği durumda ise basınç düşüşü çok daha net gözlemlendi.

Bu çalışmada, ileride yapılan kabüllerin değiştirilmesiyle ve daha gerçekçi tasarımlar kullanılarak geliştirilebilecek bir sayısal model kurulmuştur. Bu model ileride daha detaylı bir kavitasyon modellenmesiyle, sızdırmazlık elemanlarının modele dahil edilmesiyle, yüzey kalitesinin denklemlere eklenmesiyle ve/veya yağ besleme kanallarının modellenmesiyle geliştirilebilir. Ayrıca modelin doğrulanması için bir test düzeneği kurulabilir. Modelin daha gerçekçi koşulları içermesiyle yapılabilecek farklı tasarımlar, farklı operasyon koşulları ve/veya farklı yağların kullanılması simüle edilebilir ve ilerde bütün bu değişkenlerin etkisini gözlemlemek için kurulması gereken test düzeneği sayısını en aza indirgeyebilir.

1. **INTRODUCTION**

Squeeze film dampers (SFDs) are known as a type of hydrodynamic journal bearings. They have been used in rotor supporting structures of many applications such as automotive turbochargers, aircraft engines, gas turbines and compressors, industrial steam turbines to reduce vibrations due to unbalance of the rotor, reduce the loads transmitted to structural component. SFDs also improve the rotordynamic characteristic of a machine and ensure a stable operation.

A typical squeeze film damper consists of a stationary housing and outer and inner rings, roller assembly as journal. Outer ring is prevented from rotation by an anti-rotation mechanism such as retaining ring or anti-rotation pin. The stationary and rotating components are separated by a film of lubricant and lubricant is supplied to the damper clearance mostly through feed holes located in the housing. The journal center performs an orbiting motion around housing axis due to eccentricity of rotating and stationary components (residual unbalance of rotor). This motion causes the movement of oil and generates squeeze film pressure which creates fluid film reaction forces on the journal. These forces provide attenuation of transmitted bearing loads and reduction of rotor vibrations.

The damping characteristic of SFD is highly dependent on bearing and housing geometry, oil supply line and pressure, type of end sealing, lubricant type and properties, operational parameters, cavitation, and others.

Squeeze film dampers improves high performance rotor-bearing system stabilities by reducing the vibrations. However, air entrapment in oil film leads a bubbly lubricant and it causes reduction in dynamic fluid film forces and overall damping performance subsequently. Younan et al. [1] presents a new formulation of the pressure evaluation within the squeeze film damper by using nonlinear Reynolds equation pressure. This formula includes the effect of entrained air bubbles into lubricant and their results on changing lubricant properties, effective lubricant density, and viscosity. The density and viscosity formulas are modified by using air-to-oil mass ratio to introduce air bubble effect into the problem. The results are validated with the experimental data presented in work of Tao et al. [2]. The model results on load capacity and pressures are found in good agreement with experimental data. The analysis showed that air bubbles entrained in oil decreases the oil film pressure and its load capacity. Also, vibration response increased per analysis.

Xing et al. [3] set up a test rig to understand the cavitation phenomena including beginning of cavitation bubbles, formation, and evolution of them. Once cavitation begins, shape of bubbles and evolution of them are recorded by a high-speed camera while shaft position and eccentricity are tracked by help of proximity sensors. The cavitation evolution at different shaft speeds is shown in Figure 1.1. It is seen from the figure that air bubbles become more visible with increased speed. At low speeds, cavitation has more likely a fern-leaf pattern and the shape of gaseous cavitation changes to round bubbles with increasing speed since they start merging and are separated by flowing oil streams. When oil pressure falls below to vapor pressure, vapor cavitation occurs. In the experiment, vaporous cavitation begins around 2000rpm. Once speed is increased further, fluid cannot follow the shaft whirling motion due to fluid inertia and the increase in the cavitation area can be seen. Numerical simulations for the cavitation model created by same authors are validated with the experimental results.

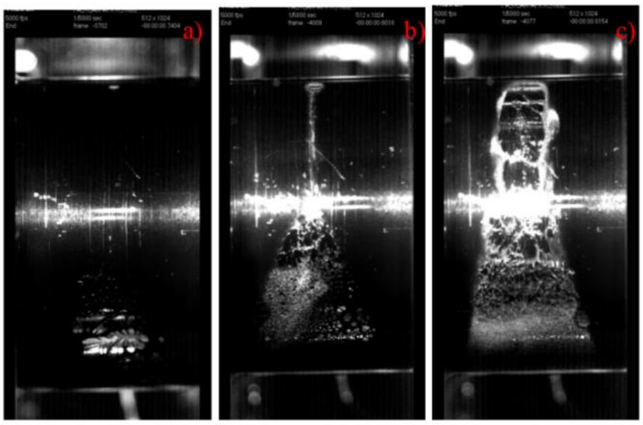

Figure 1. 1: Cavitation observation at different speeds a) 1000rpm b) 2000rpm c) 3000rpm.

The reaction force of squeeze film depends on different parameters such as operating conditions, lubricant type, and properties, bearing geometry and type of seals. The lubricant supply mechanism to the damper area is one of the critical items of SFD theory. As conventional practice, lubricant is supplied to into grooves at constant pressure and it is assumed that flow source is endless and there is no interaction between groove and film lands. Andrés [4] presented that a groove generates dynamic oil film pressures instead of isolating the film lands and ignoring the effect of central groove significantly affects the SFD dynamic forced response. In the further study of Andrés and Jeung [5], experimental measurements showed the evidence of feed groove effect on generated hydrodynamic oil film pressures. This discrepancy is occurred since a simpler physical model is used while lubricant passes from the orifices and swirls in the groove before it enters to film lands. The model introduces an effective groove depth which is the representation of a divided streamline between main vortices and film land [6]. In 2018, Andrés et al. [7] presented the measurements of the dynamic force response of SFD from two configurations. The first test is conducted with an SFD has one end flooded in a lubricant bath and other end is opened to ambient and oil flows from top to bottom by gravity. The lubricant is supplied to film lands through 3 feedholes in the second test while other parameters and operating conditions are identical in both tests. The results showed that flooded SFD generates about 30% more damping than the SFD configuration with feedholes for small amplitude orbits since feedholes causes distortion on the pressure.

The Reynolds theory of lubrication was formulated by Osborne Reynolds over a century ago and obtained based on the assumptions of constant viscosity, Newtonian lubricant, thin film geometry, negligible body force. Also, fluid inertia is neglected based on the assumption of that inertial forces are negligible relative to viscous forces [8]. However, in further studies, it is seen that inertia forces are significant at large velocities and fluid inertia effect should not be neglected. Andrés and Vance [9] analyzed the effect of fluid inertia on the force response of finite-length squeeze film dampers to circular-centered motions. An approximate finite-length SFD solution is obtained by including the inertia effects and solution is validated for small Reynolds numbers. Also, pressures are found comparable with the measured and predicted pressures presented in their previous work for an orbit radius, $\varepsilon = 0.5$.

Hamzehlouia and Behdinan [10] worked on a numerical model which includes lubricant inertia to the hydrodynamic pressure distribution. The analysis completed in this work shows the significant contribution of lubricant inertia to the fluid dynamics. Based on the results, pressure magnitude is increased, and pressure distribution is changed by including the inertia effects. The shape of pressure is seen as sinusoidal at small Reynolds numbers, but it transformed to cosine wave for larger Reynolds number. Based on the simulations, including fluid inertia attenuates steady-state vibration amplitudes of system significantly at large rotor speeds while there is no significant change at smaller Reynolds numbers. Figure 1.2 shows the vibration amplitudes at given parameters for two cases; no inertia effect and included inertia effects.

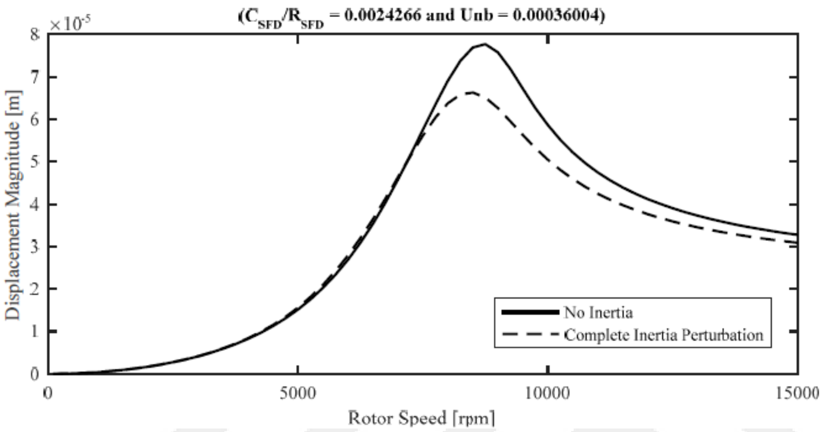

Figure 1. 2: The effect of fluid inertia on the steady-state vibration amplitudes of the rotor system - no inertia effects vs. complete fluid inertia.

In the literature, some assumptions on the cavitation pressure have been made such as cavitation pressure equals to ambient pressure if SFD is exposed to ambient air and cavitation pressure equals to vapor pressure in case of SFD is flooded in lubricant bath. Estimation of accurate cavitation pressure and definition of cavitation boundaries are the difficulties of building a cavitation model. Fan et al. [11] worked on a lubricant cavitation model by using both Gumbel's boundary condition and Elrod algorithm to compare the effect of different cavitation boundaries. The lubricant inertia effect is also explored by integrating cavitation model into fluid inertia model. Simulation results are validated with an experimental data in the literature. A sensitivity analysis performed shows the effect of cavitation boundaries and fluid inertia for different eccentricities and speeds. Results showed that cavitation region is smaller for Elrod cavitation model predictions than Gumbel's model for a smaller eccentricities and relatively larger Reynolds numbers.

There are numerous studies on the effect of fluid cavitation on the SFD performance in the literature. The ingestion of air into film land and air entrapment are significantly affected by lubricant supply mechanism, amplitude and frequency of journal motion and type of SFD end sealing. Seals are used to restrict the oil leakage from damper ends to contain the oil within the damper area during operation. They also prevent air ingestion to the damper clearance. There are different types of end sealing such as piston rings, endplates, O-rings. Levesley and Holmes [12] compared the effects of end-seals and piston rings on the dynamic capacity of an SFD by experiments. The results showed the higher damping forces are generated when piston rings are used for end sealing.

Andrés and Delgado [13] presented experimental results of a mechanical seal application. Damper housing used in the test includes a circular groove at the damper exit and normal force is applied to the mechanical end seal during test. This provided different level of sealing depending on the amount of applied force. The test includes three steps. Firstly, damper mass and structural stiffness are obtained with no mechanical seal in contact (as open ended) and no oil flow case. Second test is done to determine the dry-friction force and corresponding viscous damping characteristic by applying dynamic load to mechanical seal without oil flow. Lastly, oil is supplied to the system and dynamic loads applied to estimate the force coefficients of the system. These tests are done to understand the coefficient of squeeze film damping by subtracting the coefficient of dry friction from system force coefficient. The results showed the effect of mechanical end sealing on preventing air ingestion into the damper and oil leakage from damper ends.

The traditional squeeze film damper consists of cylindrical journal or bearing and this type of SFDs is referred to as passive SFD in the study of Mu et al. [14]. Passive SFDs have the advantages of geometric simplicity and low cost but also become disadvantageous in case of several vibration modes are occurred in the system. In the same paper, a theoretical model with the truncated cone outer ring is introduced and called active squeeze film damper. The diameter, land length and bearing radial clearance can be controlled by axial movement of ring. It controls the rotor vibrations by selecting the optimum bearing geometry.

The objective of this thesis is to develop a numerical model for a squeeze film damper based on Reynolds equation including fluid inertia. Oil film pressure and circular shaft orbit is simulated by using this model. Sensitivity analyses are completed to simulate the effect of different oil properties, operating conditions, and damper geometry. It is aimed that this model would serve as a basis for an evolving program that can be used in the development of future squeeze film dampers.

2. MATERIAL AND METHOD

Squeeze film dampers are the critical components of applications to attenuate the undesired vibration amplitudes or reduce the loads transmitted to the structural components. SFDs are used to have more stable operation of the system. They are mostly used in high speed turbomachinery.

Working principle of SFD, governing of equations, boundary conditions and numerical solution are shown in detail in following sections.

2.1. Working Principle of SFD

A stationary support or housing and journal (bearing) are the main components of a typical squeeze film damper. Bearing consists of inner ring, rolling element, cage and outer ring and outer ring is prevented from rotation by a mechanism. Anti-rotation of mechanism of outer ring is achieved by a retaining ring or anti-rotation pin. Figure 2.1 shows two type of anti-rotation mechanism for outer ring which is presented in study of Cusano and Funk [15].

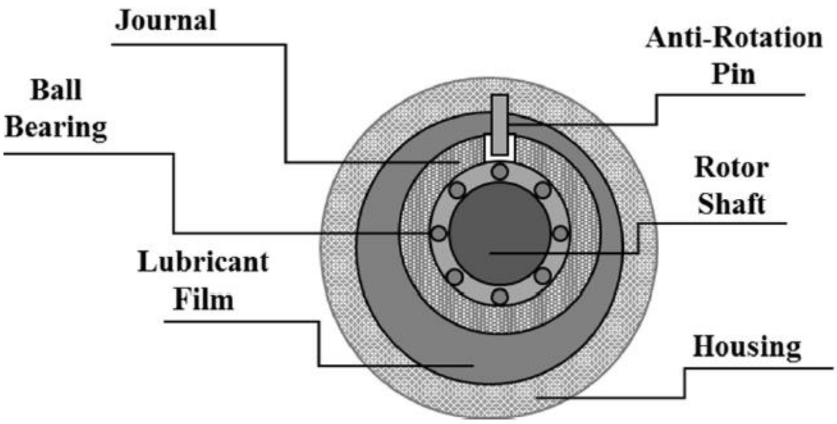

(a)

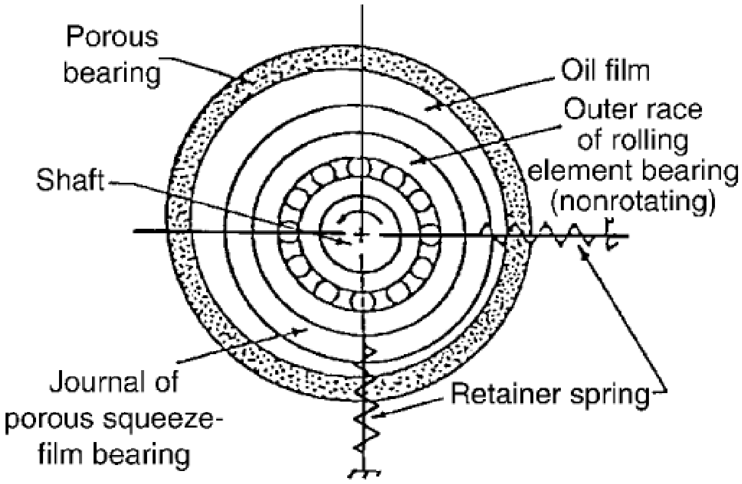

(b)

Figure 2. 1: Anti-rotation mechanism of an outer ring (a) Anti-rotation pin [10] and (b) Retainer spring.

The annular region between the stationary and rotating components are filled by lubricant and lubricant is supplied to the damper clearance mostly through feed holes located in the housing. Figure 2.2 shows the journal and bearing geometry as journal is whirling within the bearing. The component dimensions are not scaled, and they are exaggerated for better representation. The SFD geometry is defined with bearing radius *r*, radial clearance between bearing and journal *c* and the length *L*. The film thickness between journal and bearing support is shown as "*h*" and it changes as journal whirls and lubricant displaces.

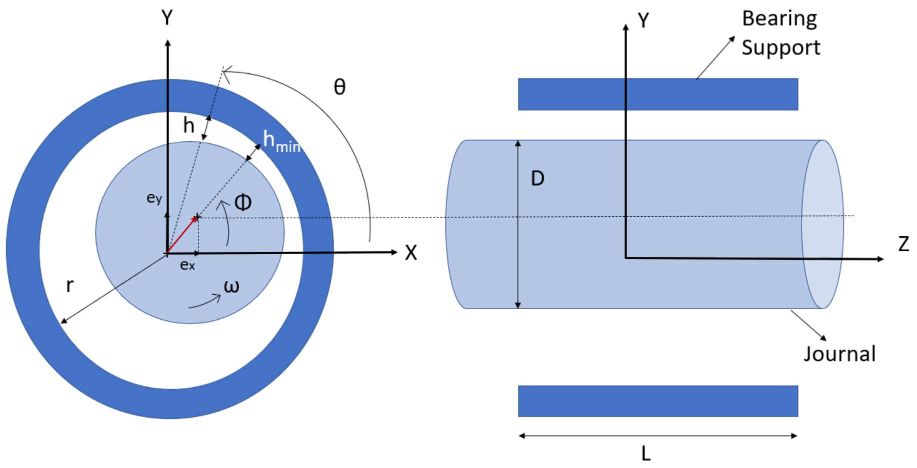

Figure 2. 2: Squeeze film damper bearing geometry and coordinate system.

The journal center performs an orbiting motion around housing axis due to eccentricity of rotating and stationary components. This motion causes the movement of oil and generates squeeze film pressure distribution which creates fluid film reaction forces on journal. These forces suppress the undesired vibration and reduce the transmitted bearing loads. The dynamic forces created by SFD are mainly dependent on damper bearing geometry, operational speed, and lubricant properties. Figure 2.3 shows the pressure distribution due to eccentricity between journal and bearing support center and whirling motion of journal around housing axis where whirling speed of journal is ω. Attitude angle and eccentricity e defines the journal position within the bearing as Φ is the attitude angle, e_x and e_y are the eccentric position of journal. Eccentric positions are found as follows:

$$e_x = ecos\Phi \tag{2.1}$$

$$e_y = esin\Phi \tag{2.2}$$

The maximum film thickness (h_{max}) occurs at $\theta = (\Phi+\pi)$ and the minimum film thickness (h_{min}) occurs at $\theta = \Phi$. θ is the angular location of the journal for an unknown oil film thickness h. Film thickness h is described by the following approximation [8]:

$$h = c - e_x cos\theta - e_y sin\theta \tag{2.3}$$

$$h = c(1 - \varepsilon cos\theta - \varepsilon cos\theta) \tag{2.3a}$$

where c is the radial clearance and ε is the eccentricity ratio of the bearing (ε=e/c).

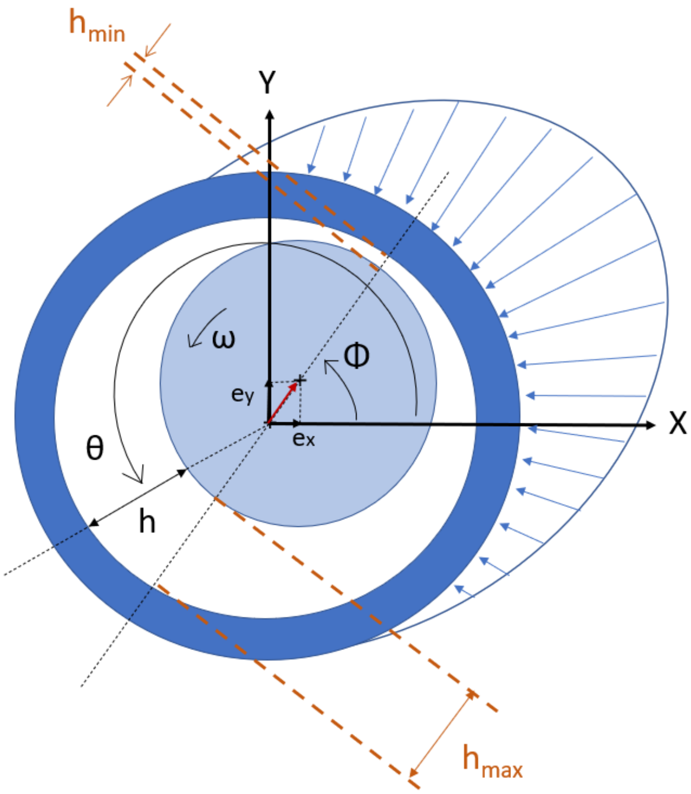

Figure 2. 3: Representation of squeeze film pressure distribution.

The whirling motion of journal squeezes oil out from the sides, and it takes a finite length of time. During this time, the fluid provides useful cushioning. It is known as load carrying capacity of the damper.

2.2. Governing Equation

Schematic model of an SFD is given in Figure 2.2. The instantaneous oil film pressure distribution can be found based on generalized Reynolds equation. Fluid inertia effect is included. To simplify the Reynolds equation, following assumptions are used:

i. Newtonian fluid – constant viscosity

ii. Incompressible fluid – constant density

iii. Laminar flow – low Reynolds numbers

iv. Thin oil film and negligible oil mass

v. Isothermal flow

vi. No material deformation

With the assumptions above, Reynolds equation can be expressed in cylindrical coordinates as follows:

$$\frac{\partial}{r\partial\theta}\left(h^3\frac{\partial p}{r\partial\theta}\right)+\frac{\partial}{\partial z}\left(h^3\frac{\partial p}{\partial z}\right)=12\mu\frac{\partial h}{\partial t}+\ \rho h^2\frac{\partial^2 h}{\partial t^2} \tag{2.4}$$

where z and θ are the axial and circumferential coordinates, r bearing radius, h oil film thickness, μ oil viscosity, ρ oil density, t time and p is the oil film pressure. The film pressure varies in both circumferential and axial directions. The first and second terms on left-hand side of the equation represent circumferential and axial flows. The right-hand side term of the equation 2.4 has only time dependent terms which are squeeze film term and fluid inertia term, respectively.

Equation 2.4 is normalized to equation 2.5 by introducing non-dimensional parameters.

$$\frac{\partial}{\partial\theta}\left(H^3\frac{\partial P}{\partial\theta}\right)+\lambda^2\frac{\partial}{\partial Z}\left(H^3\frac{\partial P}{\partial Z}\right)=12\frac{\partial H}{\partial T}+\ ReH^2\frac{\partial^2 H}{\partial T^2} \tag{2.5}$$

Dimensionless parameters are as follow:

$$H=\frac{h}{c} \tag{2.5a}$$

$$P=\frac{pc^2}{R^2\omega\mu} \tag{2.5b}$$

$$T=\omega t \tag{2.5c}$$

$$Z=\frac{z}{L} \tag{2.5d}$$

$$\lambda=\frac{r}{L} \tag{2.5e}$$

Dimensionless terms are shown with capital letters.

Equations 2.1, 2.2 and 2.3a are also normalized as follows:

$$\varepsilon_x=\varepsilon cos\Phi \tag{2.6}$$

$$\varepsilon_y=\varepsilon sin\Phi \tag{2.7}$$

$$H=1+\varepsilon cos\theta \tag{2.8}$$

where c is bearing radial clearance, ω is shaft whirling speed, L bearing axial length, ε eccentricity ratio and Re is the Reynolds number expressed with $(\rho c^2\omega)/\mu$.

2.3. Numerical Solution

Analytical solution of the equation 2.4 does not exist. To illustrate the simple numerical model, center difference method is applied to dimensionless Reynolds equation given in equation 2.5.

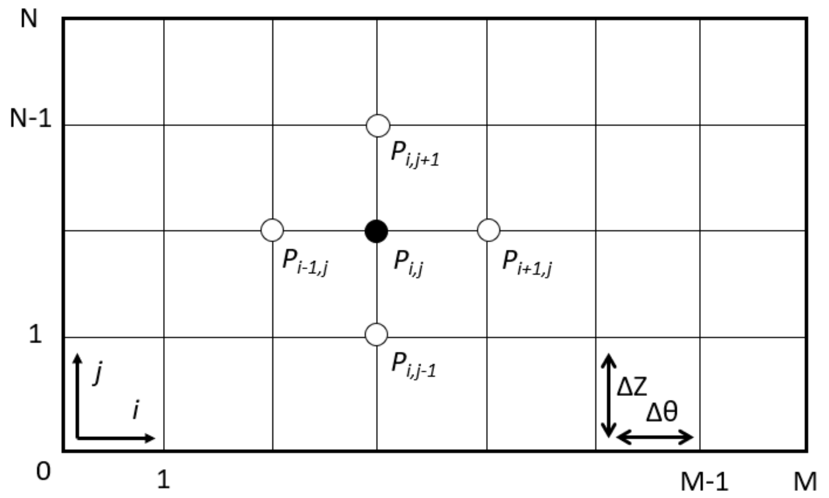

Figure 2. 4: Finite difference mesh schematic.

The internal surface of the SFD can be flattened to be a rectangular plane with 360 x 100 (M x N) grids along circumferential (θ) and axial (z) direction respectively, while element sizes, $\Delta\theta$ equals to $2\pi/M$ and ΔZ equals to L/N. Referring to Figure 2.4, center difference method is used to obtain the partial derivatives as follows:

$$\frac{\partial P}{\partial \theta} = \frac{P_{i+1,j} - P_{i-1,j}}{2\Delta\theta} \tag{2.9}$$

$$\frac{\partial P}{\partial Z} = \frac{P_{i,j+1} - P_{i,j-1}}{2\Delta Z} \tag{2.10}$$

$$\frac{\partial^2 P}{\partial \theta^2} = \frac{P_{i-1,j} - 2P_{i,j} + P_{i+1,j}}{\Delta\theta^2} \tag{2.11}$$

$$\frac{\partial^2 P}{\partial Z^2} = \frac{P_{i,j-1} - 2P_{i,j} + P_{i,j+1}}{\Delta Z^2} \tag{2.12}$$

Subsequently, equation 2.5 is numerically discretized as follows:

<u>1st term of left-hand side of equation 2.5</u>

$$\frac{\partial}{\partial\theta}\left(H^3\frac{\partial P}{\partial\theta}\right)$$

$$\frac{\partial}{\partial\theta}\left(H^3\frac{\partial P}{\partial\theta}\right) = 3{H_{i,j}}^2\ \frac{(H_{i+1,j}-H_{i-1,j})}{2\Delta\theta}\ \frac{(\boldsymbol{P_{i+1,j}}-\boldsymbol{P_{i-1,j}})}{2\Delta\theta} + \ {H_{i,j}}^3\frac{(\boldsymbol{P_{i-1,j}}-2\boldsymbol{P_{i,j}}+\boldsymbol{P_{i+1,j}})}{\Delta\theta^2} \tag{2.13a}$$

$$\frac{\partial}{\partial\theta}\left(H^3\frac{\partial P}{\partial\theta}\right) = \boldsymbol{P_{i+1,j}}\ (\frac{3{H_{i,j}}^2H_{i+1,j}}{4\Delta\theta^2}-\frac{3{H_{i,j}}^2H_{i-1,j}}{4\Delta\theta^2}+\frac{{H_{i,j}}^3}{\Delta\theta^2}) - \boldsymbol{P_{i-1,j}}\ (\frac{3{H_{i,j}}^2H_{i+1,j}}{4\Delta\theta^2}-\frac{3{H_{i,j}}^2H_{i-1,j}}{4\Delta\theta^2}-\frac{{H_{i,j}}^3}{\Delta\theta^2}) - \boldsymbol{P_{i,j}}\ \frac{2{H_{i,j}}^3}{\Delta\theta^2} \tag{2.13b}$$

<u>2nd term of left-hand side of equation 2.5</u>

$$\lambda^2\frac{\partial}{\partial Z}\left(H^3\frac{\partial P}{\partial Z}\right)$$

$$\lambda^2\frac{\partial}{\partial Z}\left(H^3\frac{\partial P}{\partial Z}\right) = \boldsymbol{P_{i,j+1}}\ [\lambda^2\ \frac{{H_{i,j}}^2}{\Delta Z^2}] + \boldsymbol{P_{i,j-1}}\ [\ \lambda^2\ \frac{{H_{i,j}}^2}{\Delta Z^2}] - \ \boldsymbol{P_{i,j}}\ [\ 2\lambda^2\ \frac{{H_{i,j}}^2}{\Delta Z^2}] \tag{2.14}$$

<u>Right-hand side terms of equation 2.5</u>

$$12\frac{\partial H}{\partial T} + \ ReH^2\frac{\partial^2 H}{\partial T^2}$$

$$12\frac{\partial H}{\partial T} + \ ReH^2\frac{\partial^2 H}{\partial T^2} = 12[\frac{{H_{i,j}}^{(t)}\ -\ {H_{i,j}}^{(t-\Delta t)}}{\Delta T} + \ Re{H_{i,j}}^2[\frac{{H_{i,j}}^{(t)}\ -\ 2{H_{i,j}}^{(t-\Delta t)}\ +\ {H_{i,j}}^{(t-2\Delta t)}}{\Delta T^2}] \tag{2.15}$$

Discretized equation 2.5 can be rearranged by using equation 2.13b, 2.14 and 2.15 with the coefficients A_1, A_2, A_3, A_4, A_5 and A_6.

$$\boldsymbol{P_{i,j}} = \frac{A_1 \boldsymbol{P_{i+1,j}} - A_2 \boldsymbol{P_{i-1,j}} + A_4 \boldsymbol{P_{i,j+1}} + A_4 \boldsymbol{P_{i,j-1}} - A_6}{A_3 + A_5} \tag{2.16}$$

where,

$$\boldsymbol{A_1} = \frac{{H_{i,j}}^2}{4\Delta\theta^2} (3H_{i+1,j} - 3H_{i-1,j} + 4H_{i,j}) \tag{2.17}$$

$$\boldsymbol{A_2} = \frac{{H_{i,j}}^2}{4\Delta\theta^2} (3H_{i+1,j} - 3H_{i-1,j} - 4H_{i,j}) \tag{2.18}$$

$$\boldsymbol{A_3} = \frac{2{H_{i,j}}^2}{4\Delta\theta^2} \tag{2.19}$$

$$\boldsymbol{A_4} = \lambda^2 \frac{{H_{i,j}}^2}{\Delta Z^2} \tag{2.20}$$

$$\boldsymbol{A_5} = 2\lambda^2 \frac{{H_{i,j}}^2}{\Delta Z^2} \tag{2.21}$$

$$\boldsymbol{A_6} = 12 \left[\frac{{H_{i,j}}^{(t)} - {H_{i,j}}^{(t-\Delta t)}}{\Delta T}\right] + Re{H_{i,j}}^2 \left[\frac{{H_{i,j}}^{(t)} - 2{H_{i,j}}^{(t-\Delta t)} + {H_{i,j}}^{(t-2\Delta t)}}{\Delta T^2}\right] \tag{2.22}$$

Equation 2.16 is the final form of oil film pressure equation and it computes the pressure at each mesh point *i* and *j* by using a matrix solver.

To improve the iterative solution, a factor, *w*, called successive over-relaxation factor (SOR) can be defined to the equation. The SOR method is used to relax the residual terms to zero by successive iteration and it accelerates the convergence process. The SOR factor is always between 1 and 2 ($1 \leq w < 2$). When *w* is equal to 1, iteration method becomes Gauss-Seidel that convergence rate of Gauss-Seidel method is much slower. The effect of relaxation factor change on convergence rate is shown in Figure 2.5 [16].

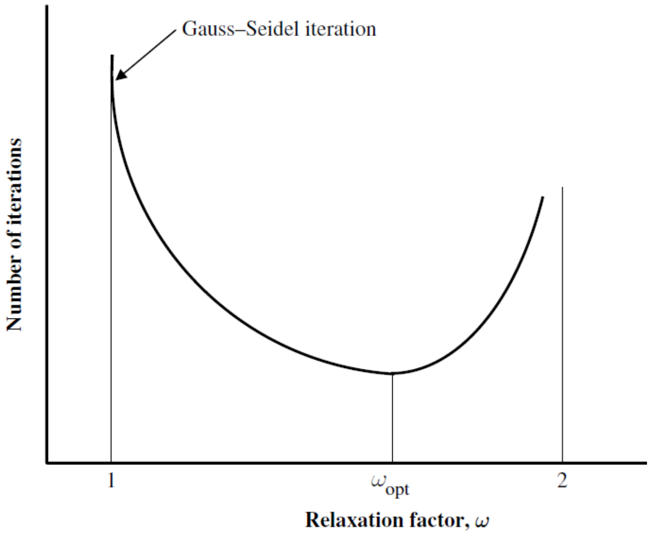

Figure 2. 5: Convergence rate of successive over-relaxation scheme.

Once SOR factor is applied to the pressure equation 2.16, equation can be rewritten as follow:

$$Pnew_{i,j} = Pold_{i,j} + \boldsymbol{w}\left[\frac{A_1Pold_{i+1,j} - A_2Pold_{i-1,j} + A_4Pold_{i,j+1} + A_4Pold_{i,j-1} - A_6}{A_3 + A_5} - Pold_{i,j}\right] \tag{2.23}$$

Equation 2.23 is used in MATLAB code for this thesis. The pressure terms can be defined as $Pnew_{i,j}$ is the new calculated pressure and $Pold_{i,j}$ is the pressure from previous iteration.

Load carrying capacity of the SFD is found by components of pressure projected along the line of centers and load carried by the lubricant film can be calculated by integrating pressure curve.

$$W_x = L\int_0^{2\pi} PR\,cos\theta d\theta \tag{2.24}$$

$$W_y = L\int_0^{2\pi} PR\,sin\theta d\theta \tag{2.25}$$

where W_x is radial load component and W_y is load in tangential direction, perpendicular to the line of centers.

A MATLAB program is developed to represent the squeeze film damper bearing model. Figure 2.6 is the flow chart illustrating the calculation of the characteristic parameters, oil film thickness, pressure, and load capacity. The code starts with the film thickness calculation which uses an initial assumption of eccentricity and attitude angle. Bearing geometry is illustrated in Table 2.1.

Table 2. 1: Squeeze film damper bearing geometry.

Bearing Parameters	Value	Unit
Bearing radius [r]	0.068	m
Bearing radial clearance [c]	0.00025	m
Damper axial length [L]	0.045	m

Once film thickness is calculated, pressure calculation begins with the initial pressure values defined for the interior nodes. Initial pressure is taken as 200kPa (2 bar). In most of the SFD applications, supply pressure is not more than 2 or 3 bar to avoid excessive weight and volume in the lubrication system. Operational parameters are given in Table 2.2.

Table 2. 2: Operational parameters.

Operation Parameters	Value	Unit
Shaft whirling speed [ω]	100	rad/sec
Oil supply pressure [P_0]	200000	Pa

In several experimental studies of Andrés and Delgado [13, 17], tests are conducted with around 1 bar supply pressure. Jeung et al. [18] presented results of single-frequency dynamic loads tests conducted on squeeze film damper sealed with piston rings. This study mainly focuses on the effects of two oil supply pressure, 0.69 bar and 2.76 bar, on the generated SFD oil film pressures and force coefficients.

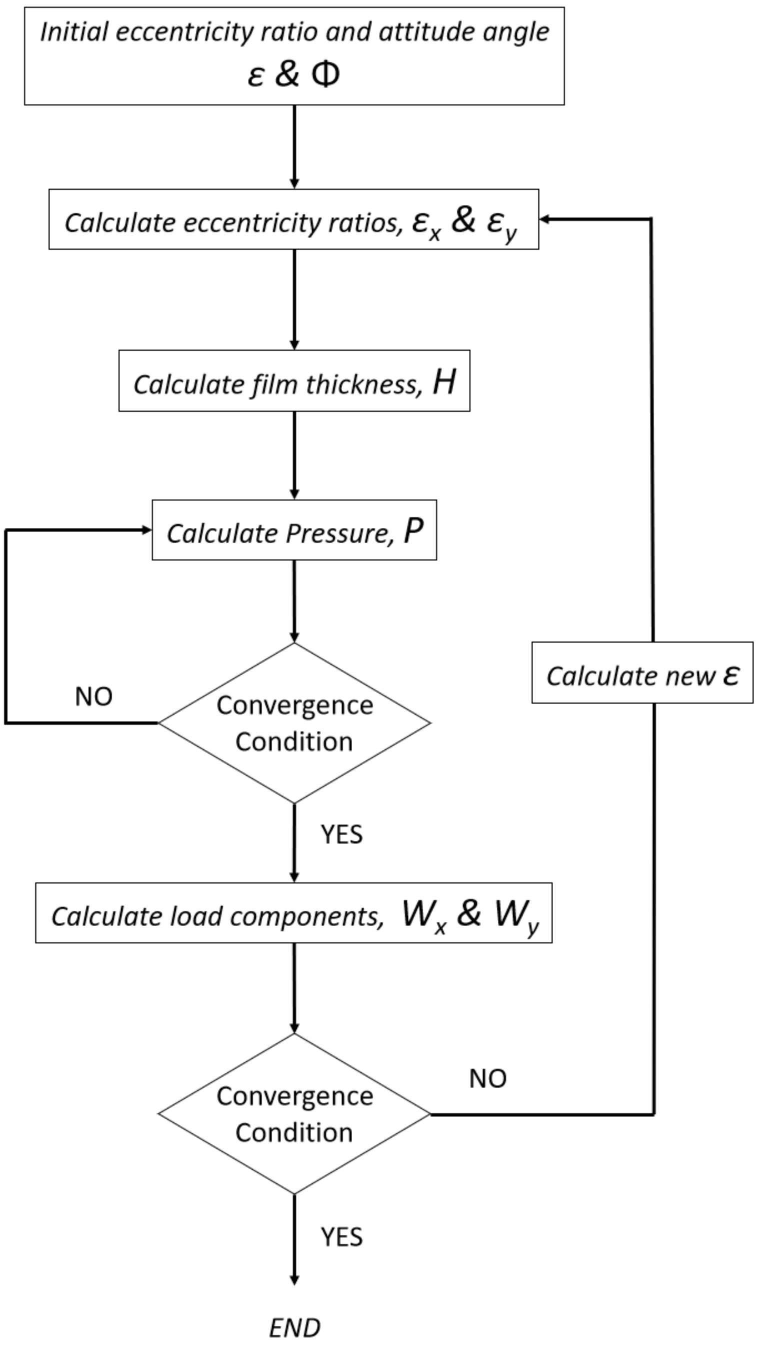

Figure 2. 6: Flow chart of calculations.

By using equation 2.23, the program predicts an updated pressure for each interior node. It starts from the entrance edge of the oil film and calculates node by node until all circumferential and axial node pressures are predicted.

The phenomena of the cavitation can be explained with the Sommerfeld pressure curve. It is known that there are very small gas bubbles (dissolved gas) in large quantities at atmospheric pressure in the oil. Non-condensable gases expand at low pressure and total volume of non-condensable gases increases. In squeeze film dampers, once the fluid pressure falls under saturation pressure of gas in fluid, gaseous cavitation occurs. The gas bubbles will grow and when oil pressure falls below to vapor pressure, vapor cavitation occurs, and bubbles are eventually separated from oil streams. Full Sommerfeld pressure distribution is shown in Figure 2.7 [3].

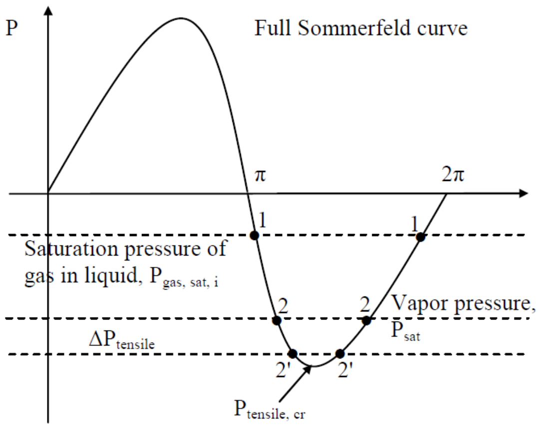

Figure 2. 7: Full Sommerfeld pressure distribution in circumferential direction.

In this thesis, pressures smaller than atmospheric pressure are set equal to atmosphere pressure, 1 bar, by assuming fluid is cavitated under atmospheric pressures. Oil is supplied to the low-pressure areas once cavitation occurs. Therefore, minimum oil pressure in the system is always set to be atmospheric pressure. This method is known as Half-Sommerfeld solution which limits the pressures to the convergent region.

The results found by Full-Sommerfeld condition are predicted with the assumptions that bearing is run free of cavitation and with lifting of journal by negative pressures in the diverging clearance section in Figure 2.8 [16]. In this study, cavitation is not neglected. In Half-Sommerfeld boundary condition negative pressures are assumed to be ambient pressure. Although, Half-Sommerfeld boundary condition violates the conservation of mass at the rupture location, load carrying capability of the bearing can be computed with acceptable accuracy. Therefore, Half-Sommerfeld approach is adopted for its simplicity. Air entrapment and oil reformation is also neglected.

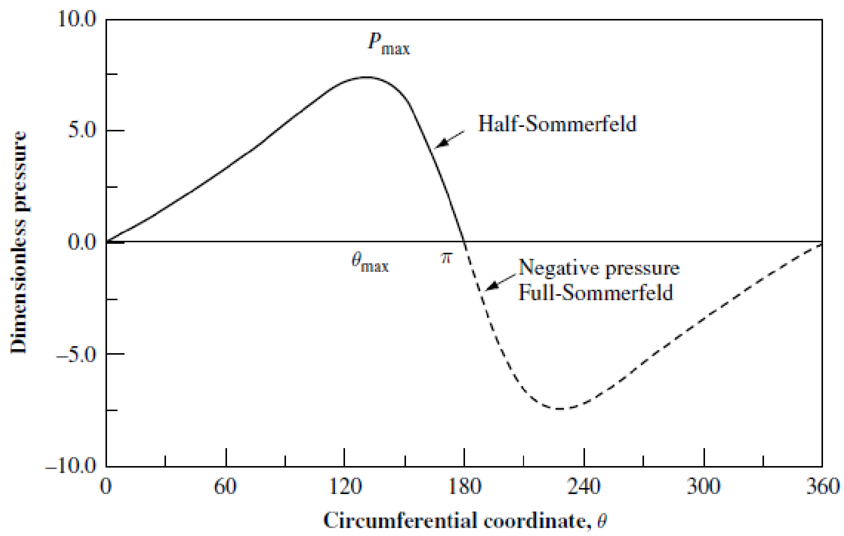

Figure 2. 8: Full and half-Sommerfeld pressure distributions.

The prediction of pressure values can be repeated until the difference between two successive iterations is found below the prescribed convergence criteria. A typical tolerance value is 0.001 for dimensionless Reynolds equation. [16] Lubricant properties used for pressure calculations are given in Table 2.3.

Table 2. 3: Lubricant properties.

Lubricant Properties	Value	Unit
Oil viscosity [μ]	0.0265	Pa.sec
Oil density [ρ]	800	kg.m^3

In this study, it is assumed that oil film pressures only damp the unbalance load of rotor and gravity force due to rotor mass. Rotor parameters are illustrated in Table 2.4. Once pressure distribution is established along the damper length and circumference, non-dimensional pressures are converted to the dimensional form. By integration of pressures using equation 2.24 and 2.25, loads carried on X and Y axis can be calculated.

The oil film pressure around the shaft generates reaction forces along tangential F_t and radial F_r directions. Including rotor inertia and gravity force, reaction forces can be calculated with equations 2.26 and 2.27.

$$F_t = Mgcos(\Phi) \tag{2.26}$$

$$F_r = [(unbal)\omega^2] - Mgsin(\Phi) - M\ddot{e} \qquad (2.27)$$

The resultant force of radial and tangential forces is equal to calculated force by integration of generated oil film pressures around shaft surface. Figure 2.9 shows the schematic of balance of reaction forces generated by oil film pressure.

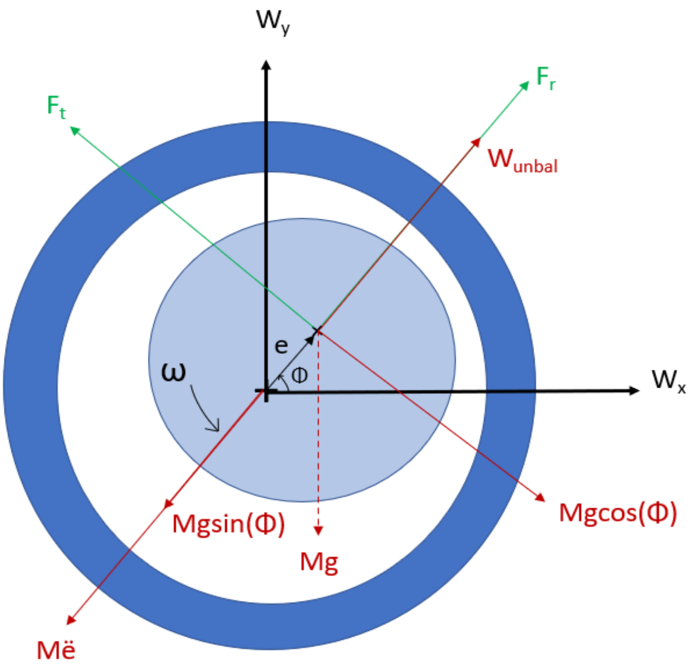

Figure 2. 9: Schematic of balance of forces.

The iteration is interrupted when the difference between the resultant force of reaction forces F_t and F_r and resultant force of calculated W_x and W_y falls under convergence criteria. The unbalance load is taken as the centrifugal force due to whirling motion of rotor with a constant whirling speed, ω. Program continues to calculate new eccentricity ratio, ε, until balance condition is obtained. Once the system is in balance for a calculated ε, program starts calculating pressure for next shaft position (attitude angle). To obtain the orbit radius, transient analysis is performed for different shaft positions.

Table 2. 4: Rotor parameters.

Rotor Geometry	Value	Unit
Mass	10	kg
Unbalance	0.003	kg.m

3. RESULTS AND DISCUSSION

3.1. Model Validation

The analytical model is validated with the experimental data originally presented in study of Tao et al [2]. In this experiment, the damper journal is centered within the housing with a fixed orbit radius. The oil supplied to the damper clearance from the left end and this end of damper is sealed with an O-ring to avoid leakage from the end. The other end of the damper opens to a plenum at constant pressure, 2 bar. This configuration creates an axial flow and pressure variation from left end of damper to the right end. Oil supply pressure relatively higher than plenum pressure to create axial flow and prevent any reverse flow of air through supply line.

The analytical model in this thesis assumes that each end of the damper is set to be at constant pressure, 2 bar. Oil flows outward to the damper ends when pressure is higher than end pressures and flows inward when pressure is less than 2 bar. The main difference between the damper system in analytical model and the test rig is that the sealing mechanism introduced in the test. One end sealing cause axial flow in one direction only and oil film creates higher pressure than analytical model. When oil flow is divided into two direction axially, pressure also decreases. Therefore, the twice as long length of the damper in the analytical model simulates the test condition. Table 3.1 shows the SFD geometry, oil properties and operating conditions used for the validation.

Table 3. 1: Analytical model and test parameters.

Parameters		Value: Analytical Model	Value: Test Conditions [2]	Units
SFD Geometry	Damper length [L]	0.0622	0.0311	m
	Bearing radius [r]	0.0647	0.0647	m
	Bearing radial clearance [c]	0.000343	0.000343	m
Oil Properties	Oil viscosity [μ]	0.0775	0.0775	Pa.sec
	Oil density [ρ]	870	870	kg/m^3
Operating Conditions	Whirling speed [ω]	52.34	52.34	rad/s
	Boundary pressure [P_0]	2	2	bar
	Eccentricity ratio [ε]	0.5	0.5	-

Since only half length of the analytical model simulates the test conditions, oil film pressure is plotted for second half of the damper. Figure 3.1 shows the pressure distribution from half length of the damper to right end of damper over the circumference of damper.

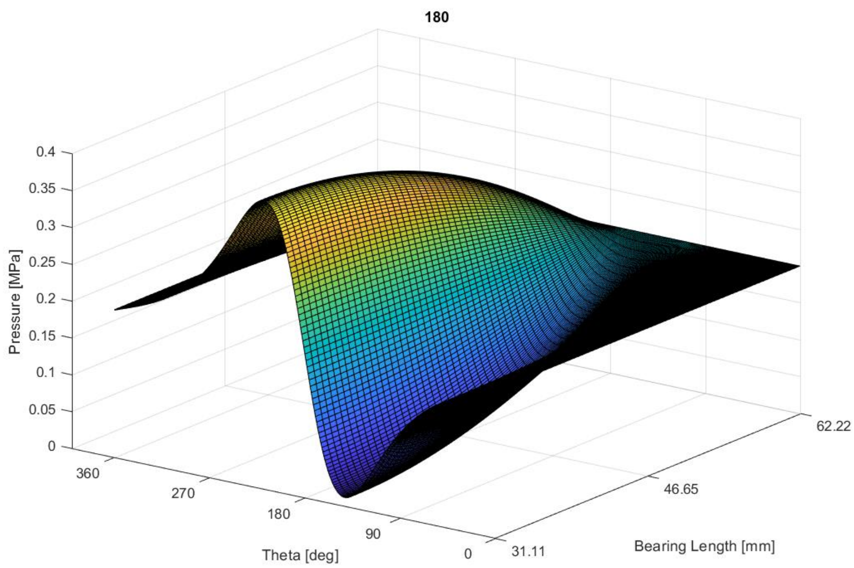

Figure 3. 1: Oil film pressure along circumference of SFD at second half of damper for analytical model.

During the test, peak to peak oil pressures and damper forces are measured for an air oil mixture. Amount of air is changed during test and effect of the air in oil on SFD performance is analyzed. Experimental data in the work of Tao et al. [2] presents the pressure distribution at half-length of damper for different amount of air in the oil. In this study, pure oil (oil without air) condition is not tested but the slope of the curve which is extracted from several air-oil mixture conditions is close to zero for lower air volume fractions. Therefore, the minimum air volume fraction (~10%) is chosen to validate the analytical model. Peak-to-peak pressure is found 3 bar for the minimum air volume fraction during the test and this data is shown in Figure 3 in the study of Tao et al [2].

The pressure plot in Figure 3.1 shows the second half of the damper in the analytical model. In the experimental work, peak-to-peak pressure is calculated for half of the damper length. To compare peak-to-peak pressures, the pressure values at half length of the plotted section of the damper in Figure 3.1 are used. Figure 3.2 shows the pressure distribution along circumference direction at ¾ length of the damper. The peak-to peak pressure is found close to 3bar which is very consistent with the experimental data.

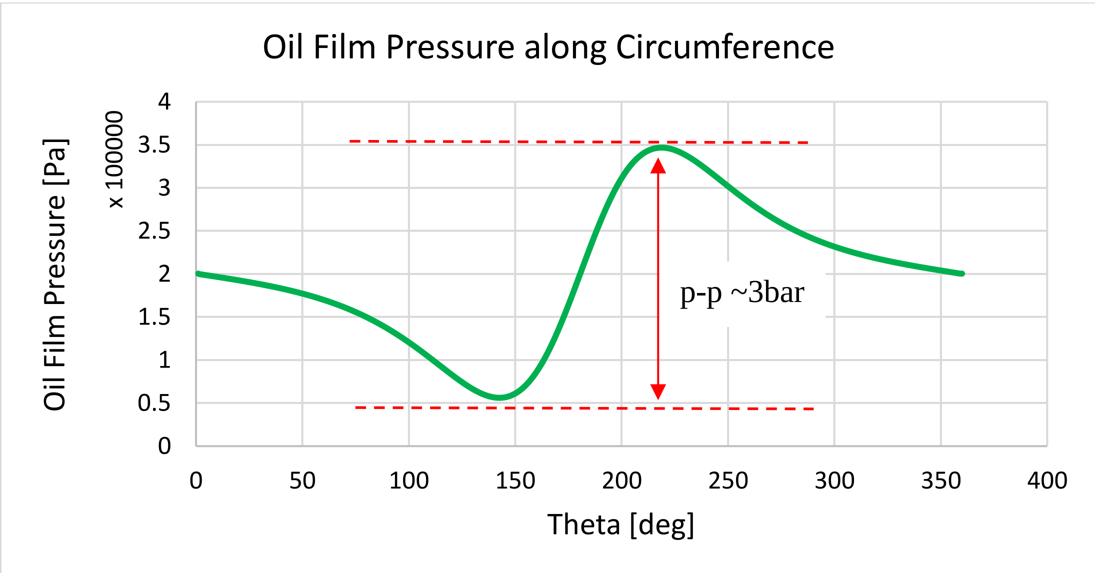

Figure 3. 2: Oil film pressure along circumference of SFD at ¾ length for analytical model.

The analytical model results showed a good agreement with experimental data in terms of pressure values and behavior of the system. This agreement validates the analytical model which can be used in development of future squeeze film dampers.

3.2. Results

After analytical model is validated, different SFD geometry and operating conditions are selected. Geometric parameters of the SFD are given in Table 2.1. Operating conditions and lubricant properties are given in Table 2.2 and 2.3, respectively. Given lubricant viscosity and density are belong to ISO VG 32 and it is used for several applications in the industry. Rotor mass and unbalance are given in Table 2.4.

The oil film pressure distribution and oil film thickness along the circumference of the SFD are calculated and plotted. Oil film thickness distribution does not change along the bearing axial length considering that film thickness is a function of circumferential location (θ) and eccentricities (e_x, e_y) per the equation 2.3. Therefore, only circumferential film thickness distribution for at any axial length of damper is plotted. Figure 3.3 shows the oil film thickness for any circumferential location when shaft is at an angle of 180˚ from the x axis. The peak values and the trend of the oil film thickness distribution do not change for different shaft positions. Only pressure profile shifts with shaft position change. Minimum oil film thickness occurs at $\theta = \Phi$ and maximum film thickness occurs at $\theta = (\Phi+\pi)$. When shaft is at 180˚ with respect to bearing center, minimum film thickness occurred at θ=180˚ and maximum film thickness occurred at θ=360˚ as expected.

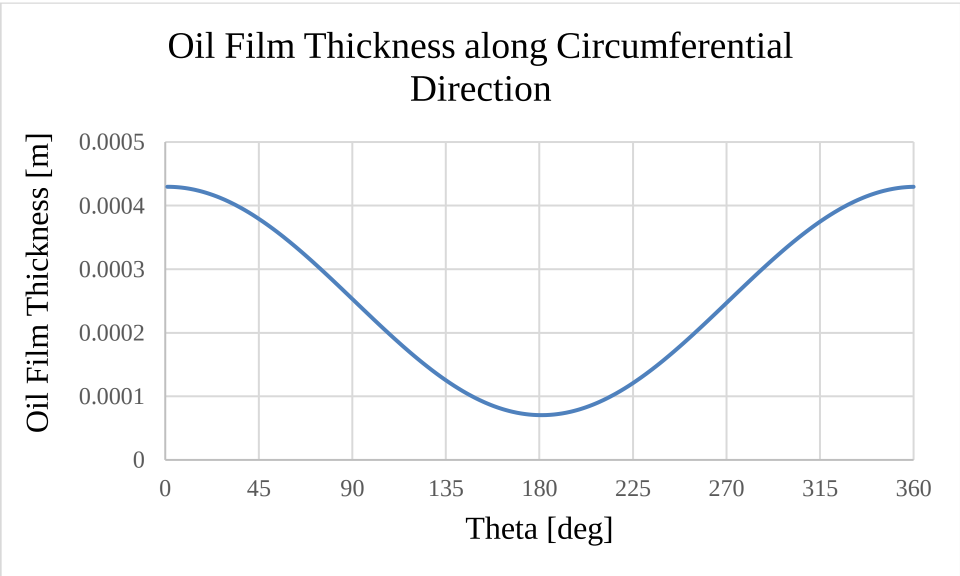

Figure 3. 3: Oil film thickness change along circumferential direction of damper for any axial location.

Oil film pressure is calculated by using equation 2.4 and plotted for rotor position at 180˚, shown in Figure 3.4. The minimum oil film pressure in the system is the ambient pressure. Pressures are limited in the convergent region by using Half-Sommerfeld method.

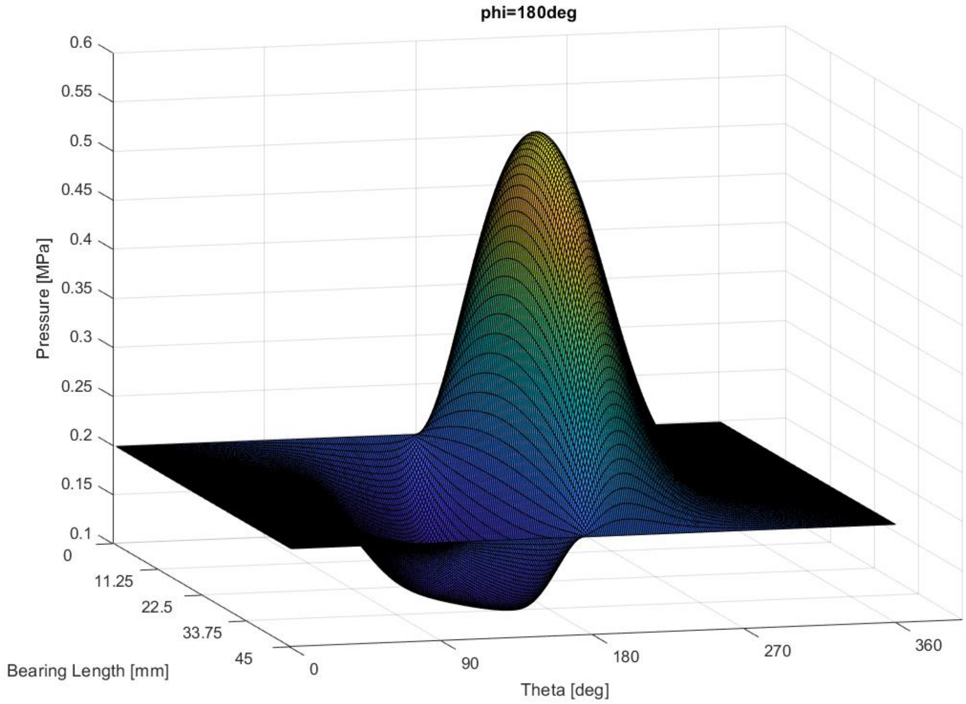

Figure 3. 4: Oil film pressure distribution over circumference and axial length of bearing at Φ=180˚.

Film thickness and pressure are plotted in same graph to show relation between minimum film thickness and maximum pressure location in Figure 3.5. Maximum pressure is seen closer to minimum film thickness location as expected.

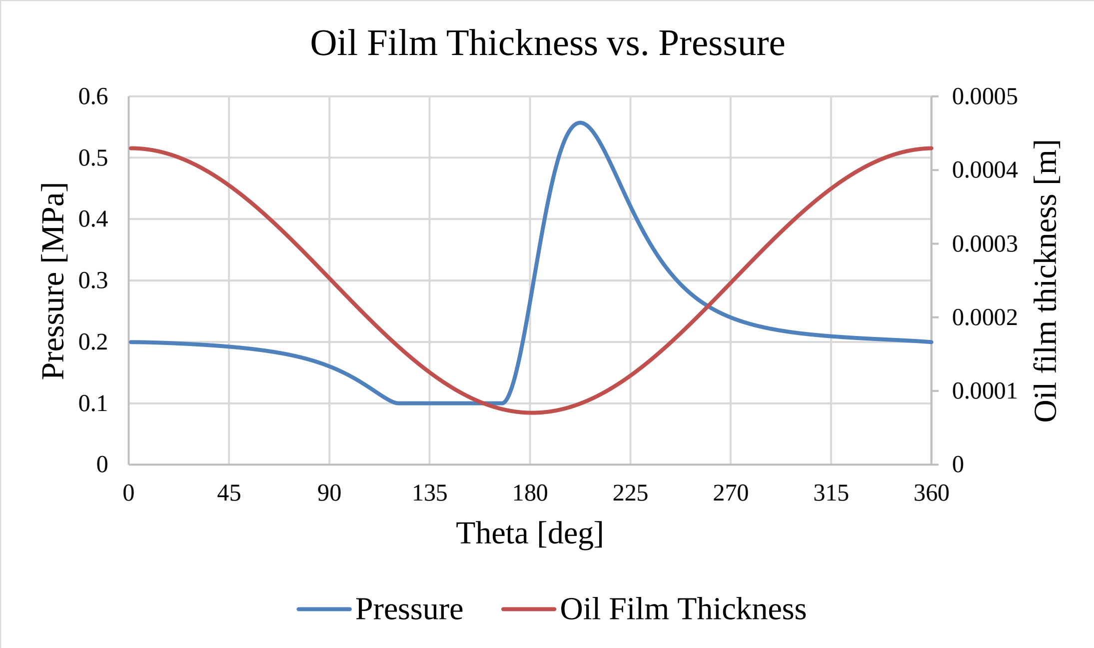

Figure 3. 5: Oil film pressure and film thickness distribution at shaft position, 180˚.

Transient analysis is performed to observe the shaft eccentricity from bearing center. The orbit response of the shaft is shown with the radial clearance in Figure 3.6. Shaft initial position relative to bearing center (Φ) and initial eccentricity (e) is given in the model and transient analysis results are plotted. Initial eccentricity given to the system is not enough high to get system to steady state response. Orbit radius increases until system reaches to balance, steady-state response. System reaches to steady-state condition when eccentricity of the journal 0.191mm (eccentricity ratio is 0.7623).

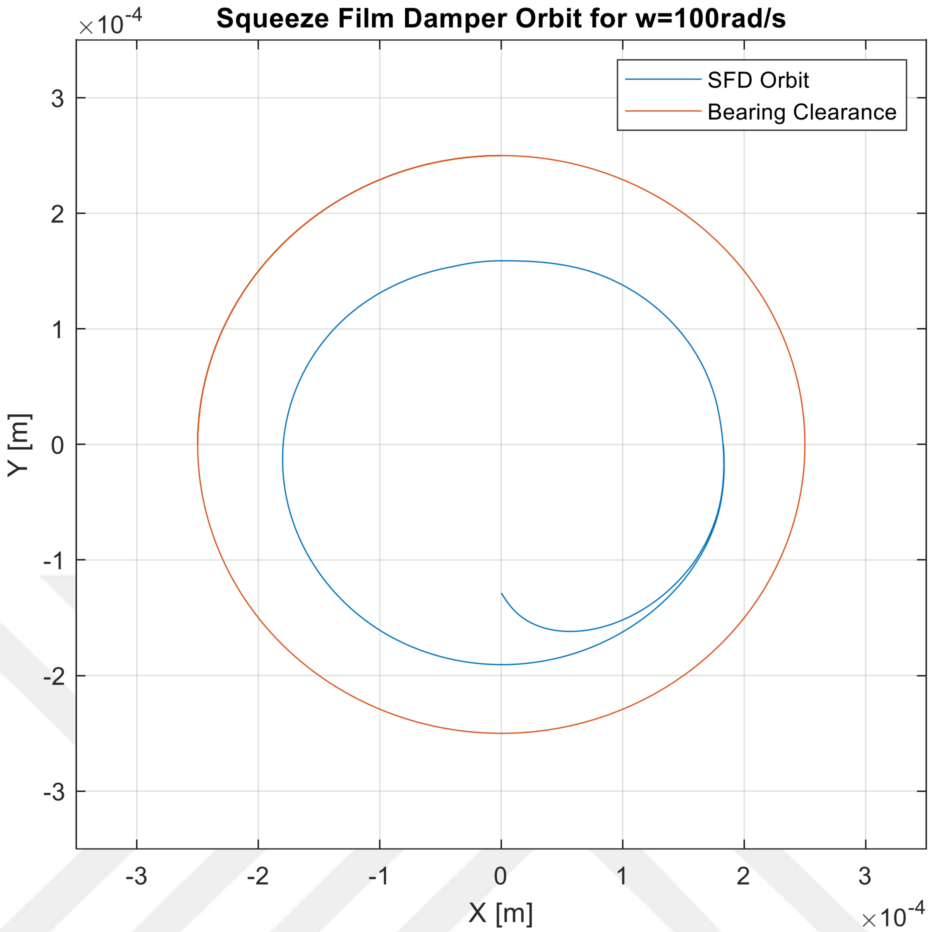

Figure 3. 6: Transient shaft response on eccentricity vs. bearing radial clearance.

3.3. Case Studies

Different cases are analyzed to see the effect of change in oil properties, operating conditions and damper geometry on oil film pressure, shaft orbital response and bearing load carrying capacity.

3.3.1. Whirling speed

The numerical model is run for higher speeds to see the effect of whirling speed on developed oil film pressure, rotor response and bearing load capacities in X and Y direction. Figure 3.7 shows the pressure distribution at half-length of the damper for different whirling speeds; 100 rad/s (955rpm), 300 rad/s (2865rpm) and 500 rad/s (4775rpm).

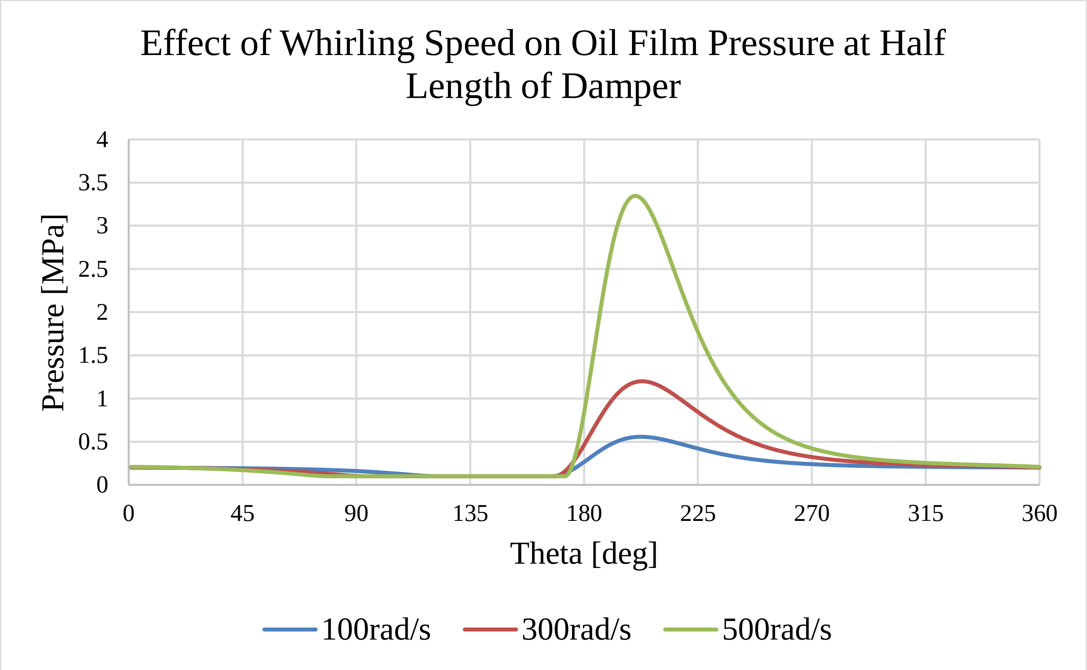

Figure 3. 7: Effect of whirling speed on developed pressure at half-length of damper at Φ=180˚.

It is seen from the figure that higher journal whirling speeds cause pressure increase. The numerical model in this thesis assumes that oil pressure damps only unbalance load and gravity force due to rotor weight. Rotor unbalance load is strictly dependent on the whirling speed and unbalance. Therefore, once speed increases, unbalance load also increases. Increased unbalance load results with higher oil film pressures since oil will be squeezed more between journal and housing surface and it will create more reaction force. With pressure increase, the integrated area becomes higher and load carrying capacity increases. Figure 3.8 shows the reaction forces in horizontal and vertical directions. For higher speeds, increase in Wx and Wy can be seen clearly. Figure 3.7 is taken when journal is at 180˚ angle from X-axis. Based on the Figure 2.9, horizontal force is in balance with radial force in equation 2.27. Generated radial force is highly dependent on the unbalance load since unbalance load is acting in radial direction and it is only component of F_r. Therefore, when shaft is at 180˚ angle from X-axis, the effect of whirling speed increase is more significant for horizontal force than vertical force.

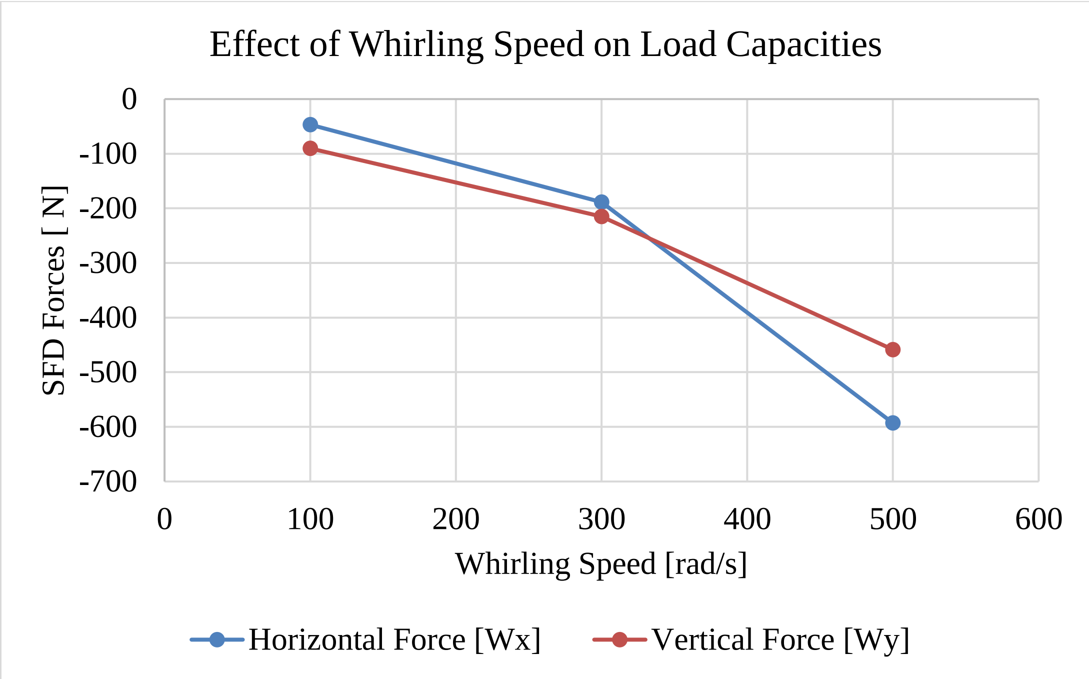

Figure 3. 8: Effect of whirling speed on generated reaction forces at half-length of damper at Φ=180˚ .

Transient analysis is also performed to see the effect of whirling speed on rotor response. Three different operating speeds, 100 rad/sec, 300 rad/sec, 500 rad/sec, are conducted and orbital responses are shown in Figure 3.9. In all cases, final orbit become circular once it reaches to steady-state condition. The orbit centers are not aligned with geometric center (0,0) of housing. The reason is that rotor weight is included to the numerical model with the equations 2.26 and 2.27.

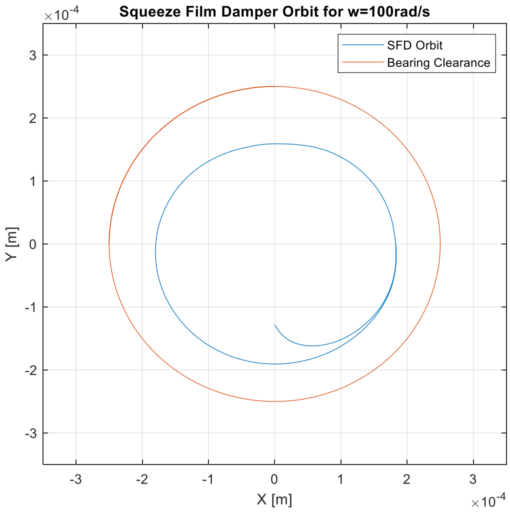

a)

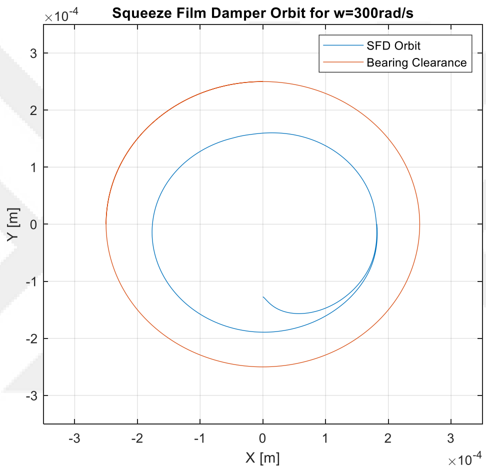

b)

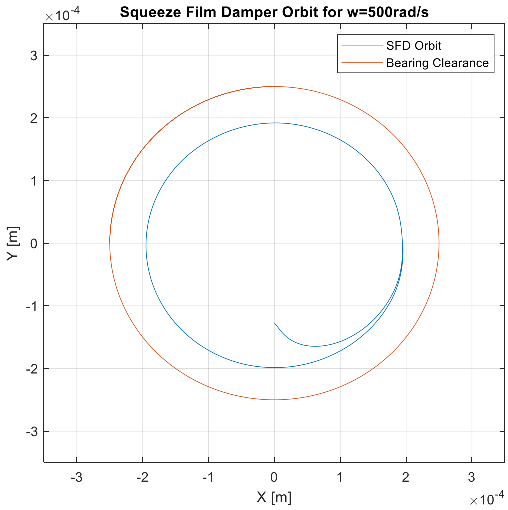

c)

Figure 3. 9: Effect of whirling speed on shaft response at half-length of damper, a)100 rad/s b)300 rad/s c)500 rad/s.

Figure 3.10 shows the orbits of all three cases together to see the effect on whirling frequency of journal on the rotor response. Due to increase on unbalance load, journal reaches the steady-state response at higher eccentricities. There is no significant increase on the eccentricity between 100 rad/s and 300 rad/s while the difference of the case for 500 rad/s from smaller speeds is clearly seen. It can be explained with that when journal speed increases, rotor gets in balance at higher eccentricities which squeezes oil more. Table 3.2 shows the maximum journal eccentricity from bearing center and eccentricity ratios for each analyzed whirling speeds at Φ=180˚.

Table 3. 2: Maximum rotor eccentricity at steady-state condition for different speeds at Φ=180˚.

Whirling speed [rad/sec]	Eccentricity [mm]	Eccentricity Ratio
100	0.191	0.7623
300	0.189	0.7573
500	0.199	0.7978

From Figure 3.10, it is also seen that orbit center gets closer to geometric center of bearing housing even rotor moves more outward from center.

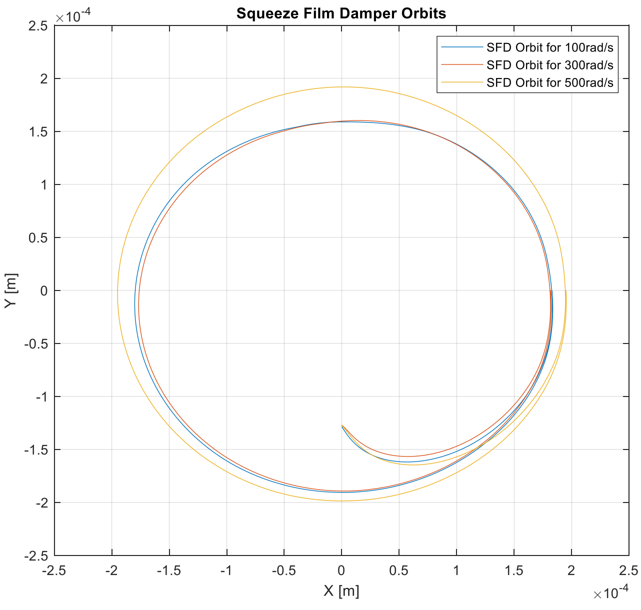

Figure 3. 10: Journal orbits for different speeds.

3.3.2. Fluid inertia effect

In classical lubrication theory, inertial forces are assumed negligible comparing to viscous forces in hydrodynamic journal bearings for the thin film regions [10]. However, in modern systems, inertia effects of the lubricant are included to the design and analysis considering the increased velocities and sizes of rotors. The validated model includes the fluid inertia to simulate the experimental conditions. Figure 3.11 shows the effect of fluid inertia on shaft orbital response for different whirling frequencies, 100 rad/s and 500 rad/s.

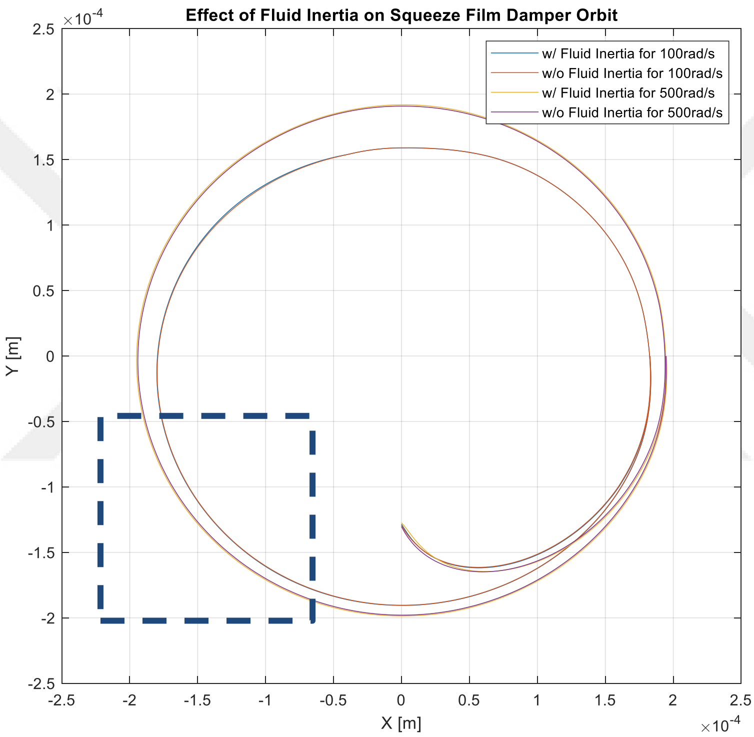

Figure 3. 11: The effect of fluid inertia on journal orbit for different frequencies.

Inertia effect cannot be understood from Figure 3.11 easily since speed effect is more significant than fluid inertia. Figure 3.12 shows a closer view of orbits given in Figure 3.11 within dashed line. For both whirling speeds, 100 rad/s and 500 rad/s, rotor orbit radius is slightly higher for the cases that fluid inertia is included. The increase is more significant for the higher speeds.

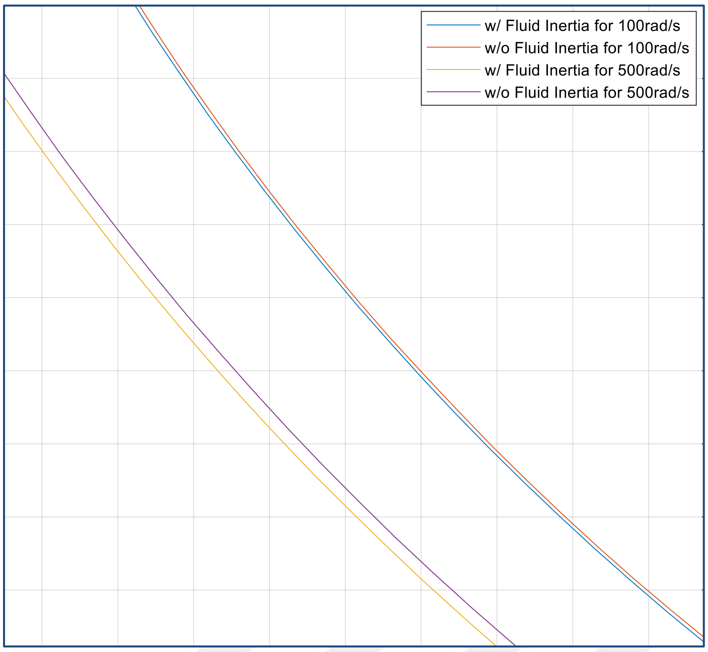

Figure 3. 12: Closer view of shaft orbital responses for different whirling frequencies.

Figure 3.13 shows the effect of fluid inertia on generated oil film pressure where whirling speed is 500 rad/s. Fluid inertia does not significantly affect the oil film pressure for these speeds. It increases peak pressure slightly but there is no significant change on the shape of the pressure profile. For higher speeds, fluid inertia effect is more significant on pressure. Hamzehlouia and Behdinan [10] studied the effect of fluid inertia on SFD performance for different Reynolds numbers. Their model and results showed that fluid inertia has significant contribution to the fluid dynamics. Fluid inertia provided pressure magnitude increase and peak pressure location shifted in direction of minimum film thickness location.

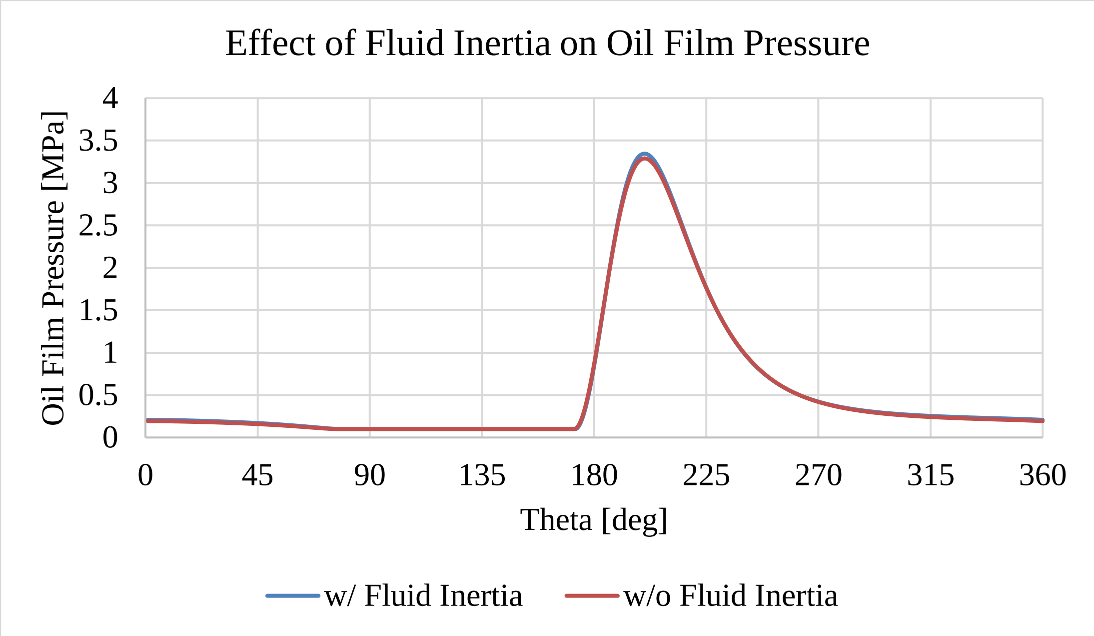

Figure 3. 13: The effect of fluid inertia on oil film pressure for w=500 rad/s at Φ=180˚.

In the most studies published in the past, fluid inertia is not included to the SFD models and it is assumed that inertial forces are very small comparing to viscous forces. In recent studies, it is seen that effect of fluid inertia become very significant for higher speeds turbomachinery and should not be neglected. In this thesis, very small Reynolds numbers are analyzed so significant effect of fluid inertia is not observed.

3.3.3. Oil viscosity

In the main model, oil is selected as ISO VG 32 and viscosity of the used oil is 0.0265 Pa.sec for temperature 48˚C. Two different viscosities are studied to represent the effect of temperature change in SFD. ISO VG32 type of oil is comparable with SAE 10W. Based on Vogel viscosity equation and available constants for SAE 10W type of oil, viscosities are found as 0.0371 Pa.sec and 0.0071 Pa.sec at 40˚C and 90˚C, respectively. Figure 3.14 shows the effect of viscosity on oil film pressure by analyzing three different temperature cases, relatively different viscosities. Higher temperatures mean smaller viscosities and when viscosity becomes lower, developed pressure increases at a higher rate whereas load carrying capacity of the fluid film remains constant.

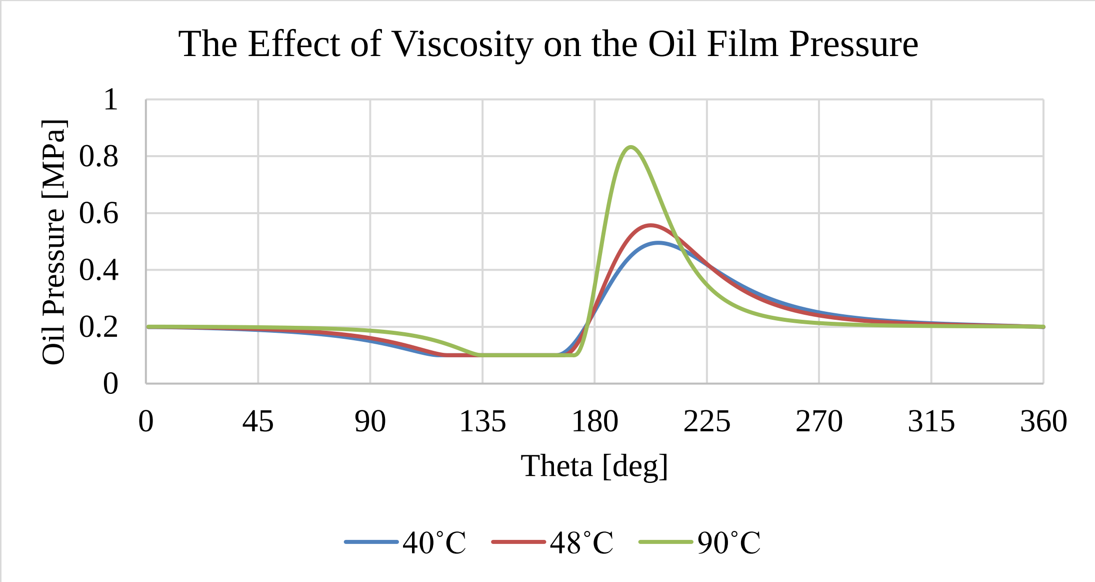

Figure 3. 14: The effect of viscosity on oil film pressure at Φ=180˚.

Due to eccentric motion of journal, significant amount of work done on the fluid and it increases the oil temperature. When oil temperature become higher, viscosity decreases, and effectiveness of damper is also decreasing. Therefore, the increase in the pressure seen in Figure 3.14 for smaller viscosities is not expected. However, in this numerical model, oil film thickness behavior changes rapidly since eccentricity changes to get system in balance under unbalance load and rotor weight. The eccentricities are shown for three different viscosities, temperatures in Figure 3.15.

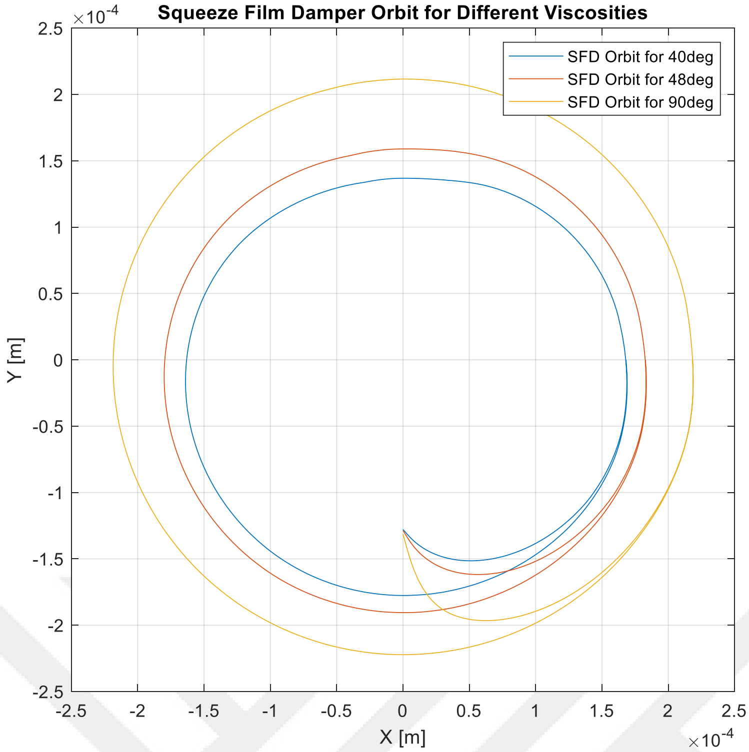

Figure 3. 15: The effect of viscosities on shaft orbit radius.

The validation model is run at fixed eccentricity to compare the results with experimental study which means oil film thickness distribution does not change during operation. The effect of viscosity change can be seen better when oil film thickness distribution is constant. Figure 3.16 shows the oil film pressure distribution at half-length of damper when shaft is at 180˚ angle from x-axis for two different viscosities, 0.0775 Pa.sec and 0.0375 Pa.sec. It is seen that peak pressures decrease for lower viscosities, higher temperatures as expected.

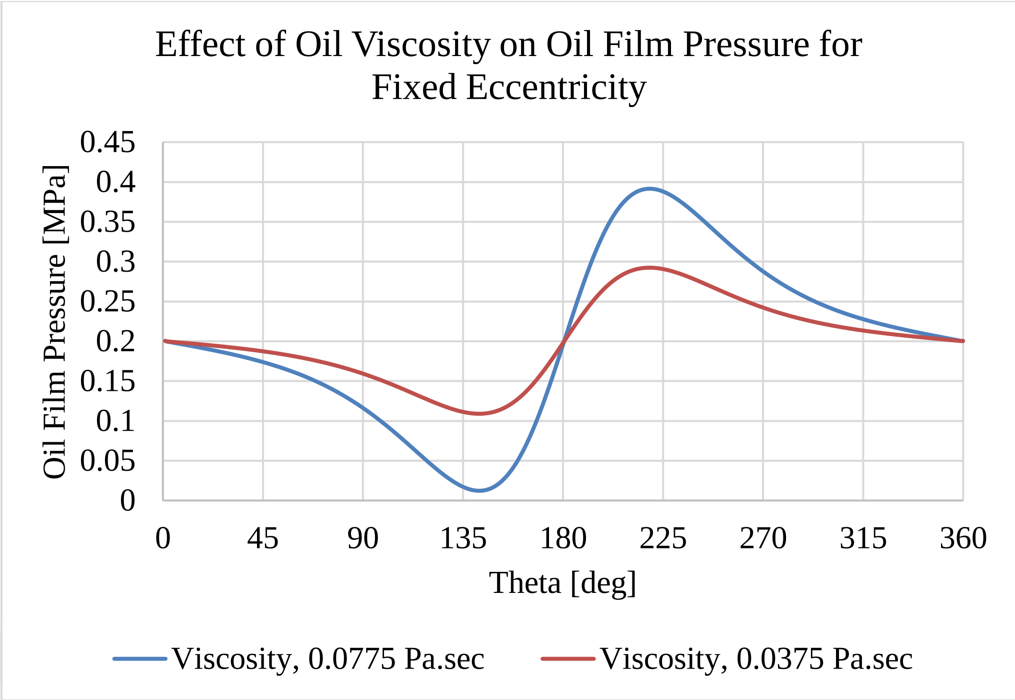

Figure 3. 16: The effect of oil viscosity on oil film pressure for a fixed eccentricity at Φ=180˚.

3.3.4. Rotor mass

The gravity force due to rotor mass is also included to the numerical model. Figure 3.17 shows the effect of rotor mass change on oil film pressure.

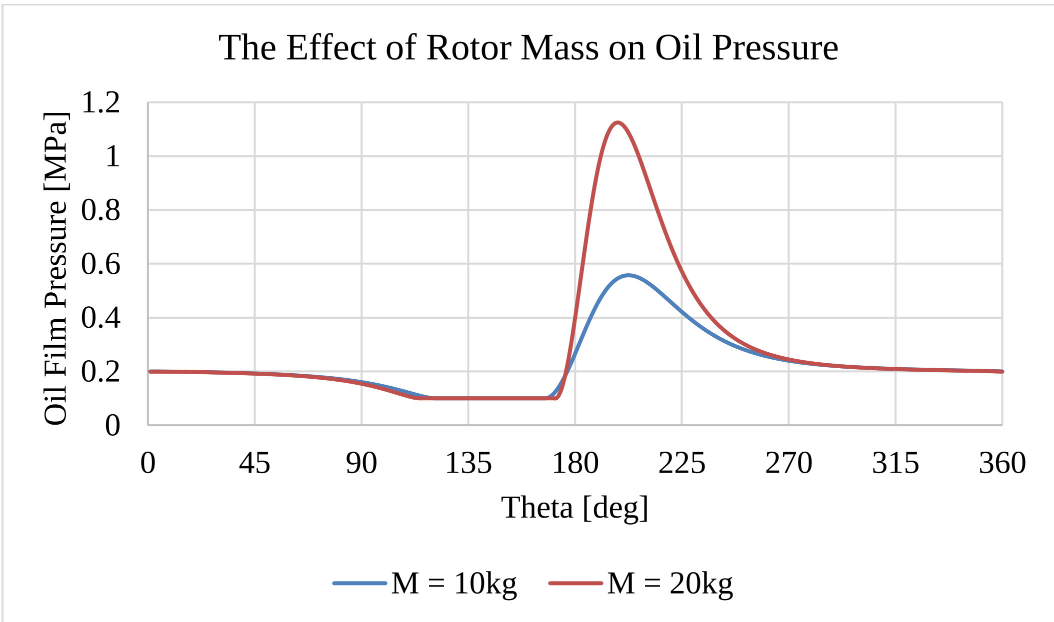

Figure 3. 17: The effect of rotor weight on oil film pressure at Φ=180˚.

Oil film pressure increases when rotor mass is increased from 10kg to 20kg. The reason of this change is that when rotor weight is increased, journal squeezes oil more at initial position. When it starts whirling, the stabilization of rotor is achieved at higher orbit radius which is shown in Figure 3.18. Since the shaft rotates at higher eccentricities, oil squeezing creates more pressure for higher rotor weights.

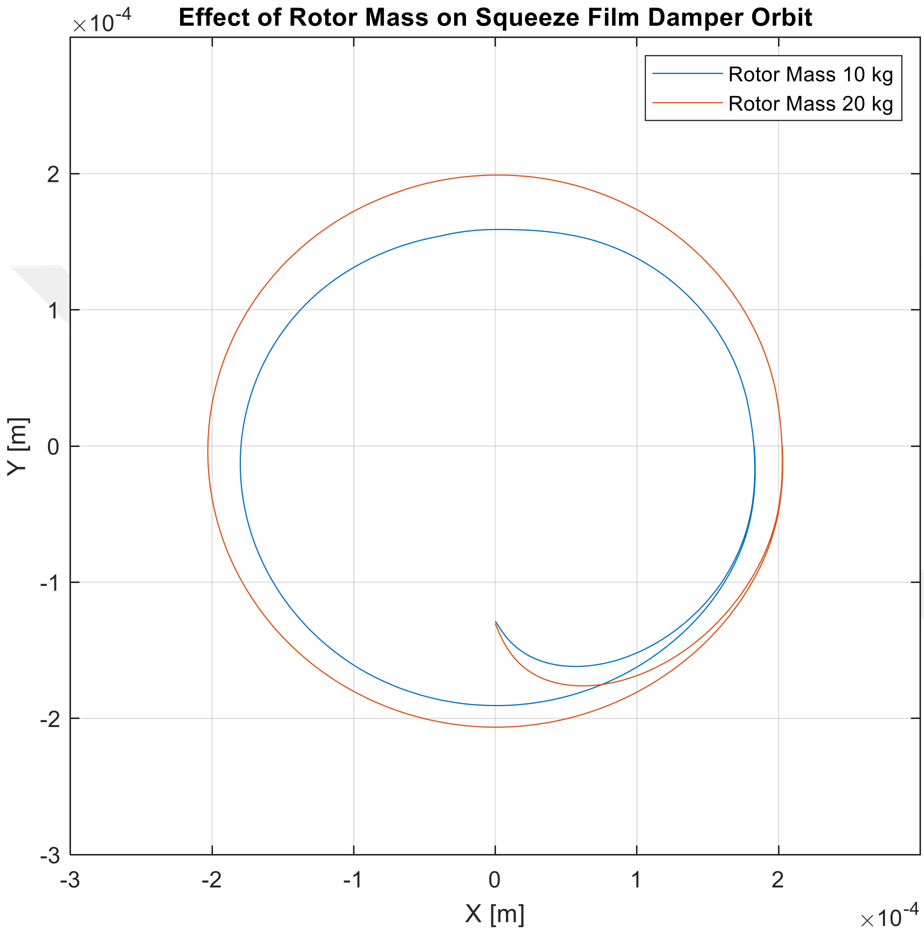

Figure 3. 18: The effect of rotor weight on shaft orbit radius.

3.3.5. Center groove

Various lubricant distribution methods can be applied to the SFDs depending on the application. In most of the studies found in literature, deep groove located at middle of the housing and lubricant is supplied to into grooves at constant pressure. It is assumed that flow source is endless and there is no interaction between groove and film lands. In the further studies, experimental measurements showed the evidence of feed groove effect on generated hydrodynamic oil film pressures. This discrepancy is occurred since a simpler physical model is used while lubricant passes from the orifices and swirls in the groove before it enters to film lands. Groove is also used to have more stable operation. Once groove is added to the system, damper length becomes shorter and unit loading increases [16].

In this thesis, SFD defined in numerical model has constant and continuous bearing clearance. To understand the effect of any circumferential groove, model is updated by adding a simple centered groove with a specific length and depth. Figure 3.19 shows groove geometry used in numerical model. Groove depth is set to 2 times of damper radial clearance and groove base length is set to 1/5 of total damper length.

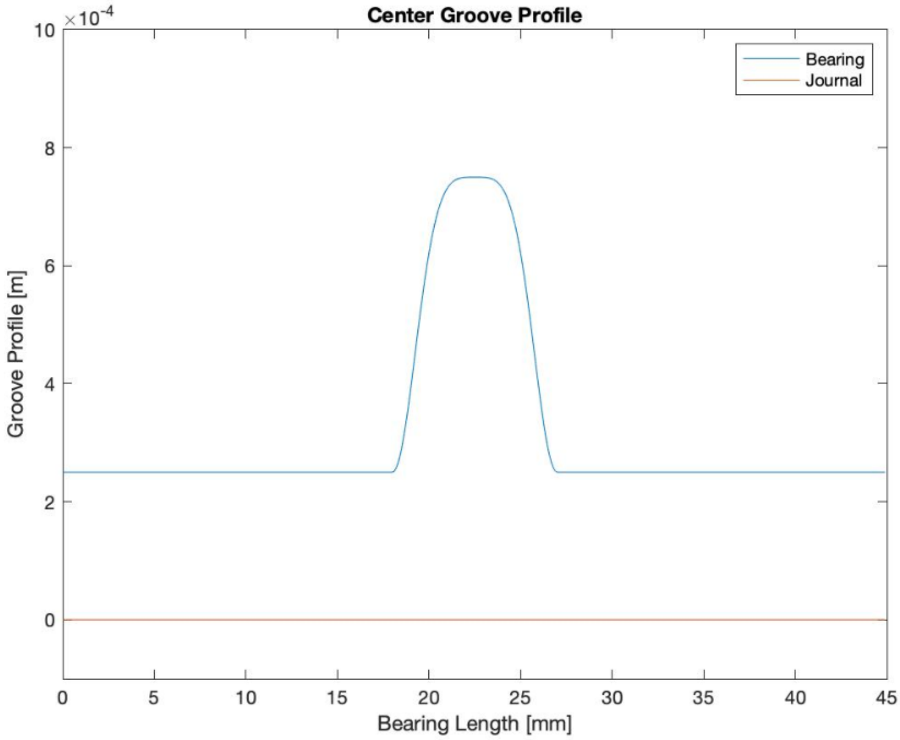

Figure 3. 19: Centered groove geometry.

The center groove divides the flow into two separate dampers which peak pressures occur at two locations. Figure 3.20 shows the oil film pressure distribution for two cases: main damper with no groove and damper with center groove.

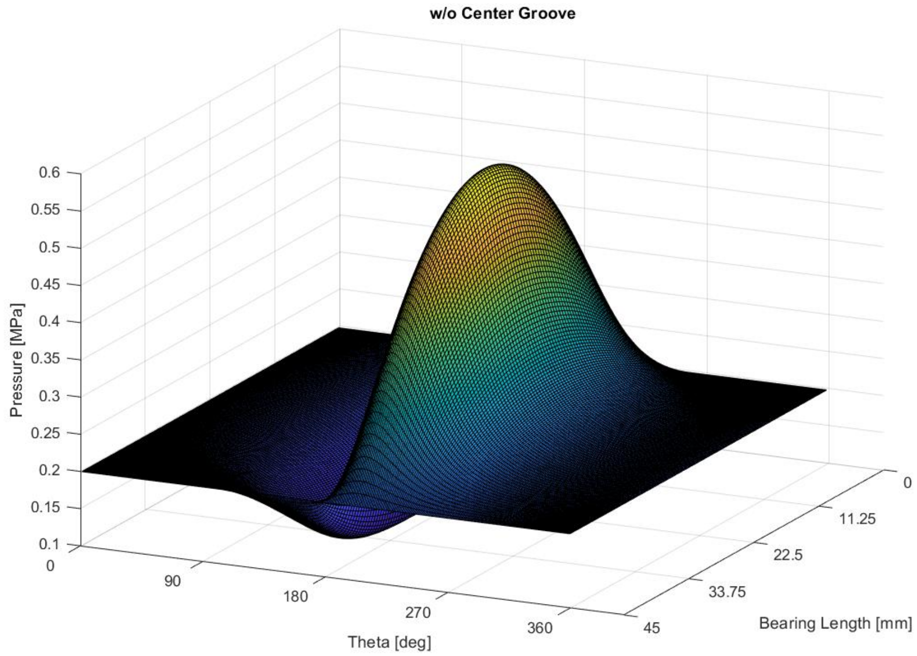

a)

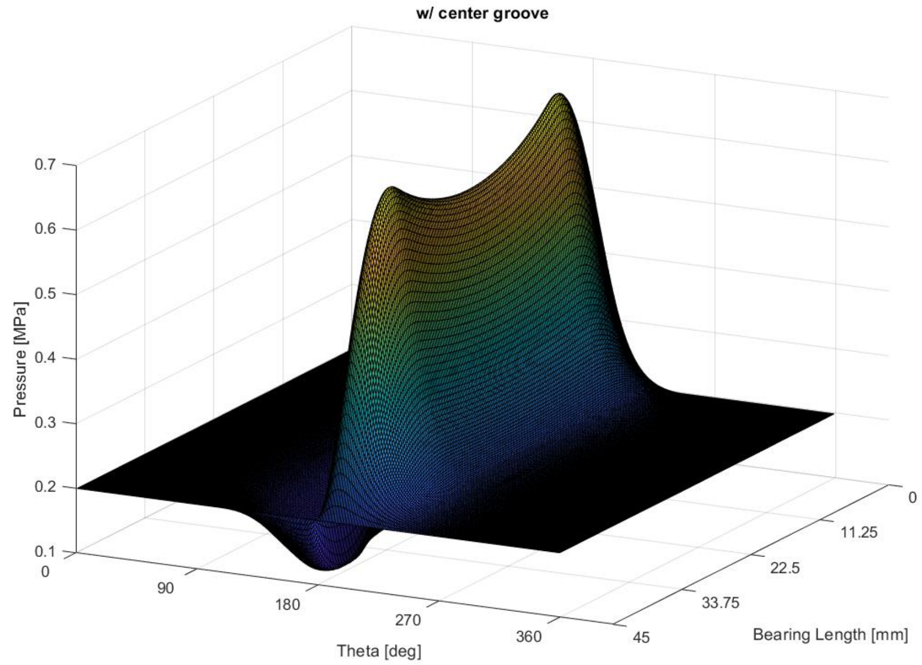

b)

Figure 3. 20: Oil film pressure distribution for a) no-groove b) with center groove design.

Based on Figure 3.20, it is seen that peak pressure does not occur at half of the damper length for grooved design unlike no-groove design. Because of the groove, pressure decreases on this area and peak pressure locations shift towards to damper ends. Once oil film pressure decreases on groove location, film thickness also decreases. Since unbalance load is always balanced with reaction forces due to oil pressure, system reaches to balance condition at higher eccentricities. The orbit change due to grooved design can be seen in Figure 3.21.

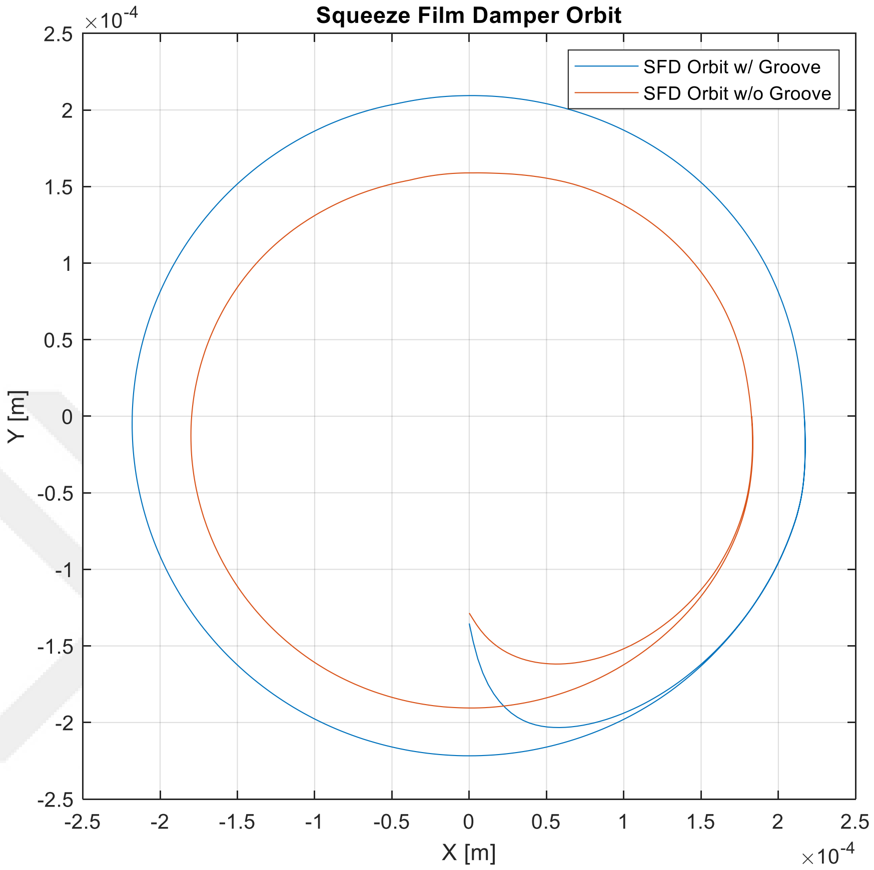

Figure 3. 21: SFD orbit change for grooved design.

Pressure decrease due to groove can be seen more clearly when journal is operating at fixed eccentiricity. Figure 3. 22 shows the pressure distributions at θ=225˚ when shaft is at angle of 180˚ from x-axis. While no-groove design reaches to peak pressure at half of damper length, the system with center groove has two peak pressures slightly at both side of groove location. Pressure decrease can be seen in Figure 3.22 clearly while two peak points of pressure due to divided flow can be seen clearly in Figure 3.20.

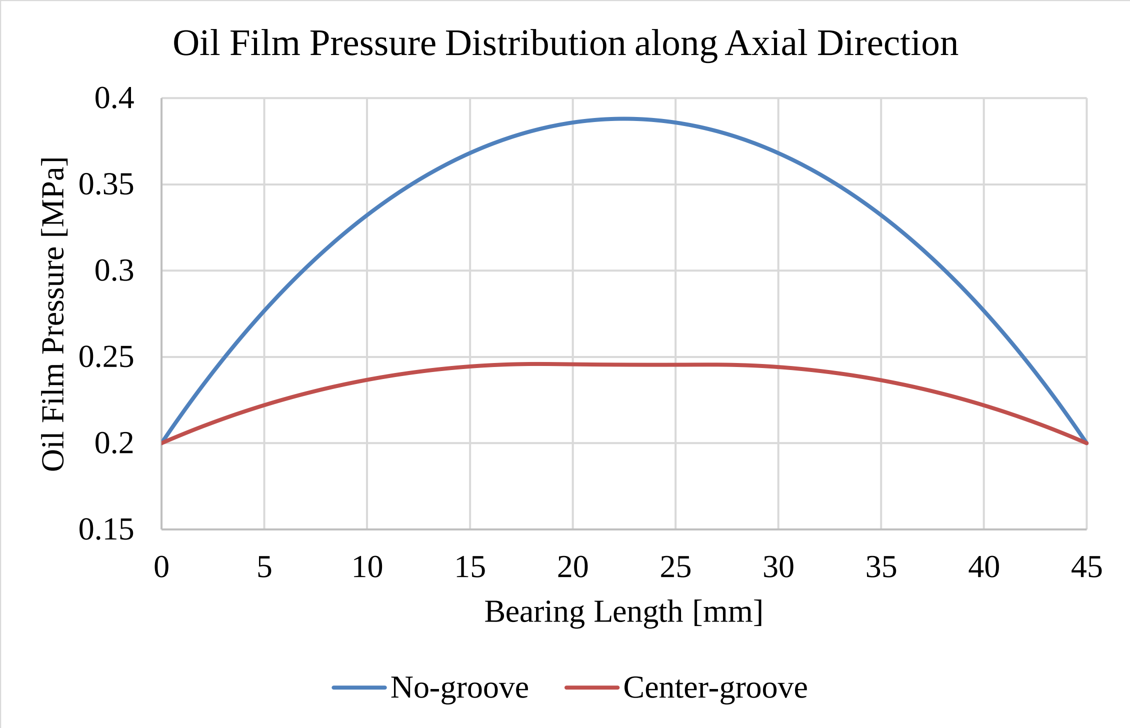

Figure 3. 22: Oil film distribution along axial direction for both no-groove and center-groove design.

4. CONCLUSIONS AND RECOMMENDATIONS

The numerical SFD model presented in this thesis is validated with an experimental study and sensitivity analysis are conducted to see the effect of any parameter change for operational, geometrical or on lubricant properties. According to obtained results;

1. The analytical model results showed a good agreement with experimental data available in literature in terms of pressure values and behavior of the system.

2. The maximum oil pressure magnitude occurs at closest to the minimum film thickness location for each shaft position.

3. Rotor unbalance load is strictly dependent on the whirling speed and unbalance. Therefore, once speed increases, unbalance load also increases. Increased unbalance load results with higher oil film pressures since oil will be squeezed more between journal and housing surface and it will create more reaction force.

4. When pressure increases, the integrated area become higher and load carrying capacity increases.

5. For all three different operating speeds, final journal orbit become circular once it reaches to steady-state condition.

6. Since rotor weight is included to the model, the orbit centers are not aligned with geometric center (0,0) of housing. It is slightly below the geometric center. For higher speeds, orbit center gets closer to geometric center.

7. For both whirling speeds, 100 rad/s and 500 rad/s, rotor orbit radius is slightly higher for the cases that fluid inertia is included. The increase on eccentricity is more significant for the higher speeds.

8. Fluid inertia does not significantly affect the oil film pressure for analyzed speeds, small Reynolds numbers. It increases peak pressure slightly but there is no significant change on the shape of the pressure profile.

9. Increase in rotor weight causes that journal squeezes oil more at initial position. When it starts whirling, the stabilization of rotor is achived at higher orbit radius. Since the shaft rotates at higher eccentiricities, oil squeezing creates more pressure for higher rotor weights.

10. In center groove design, flow is divided into two separate damper. Once oil film pressure decreases on groove location, film thickness also decreases. System reaches to balance condition at higher eccentricities.

This numerical model can be a basis for an evolving program can be used in the development of future squeeze film dampers.

This model can be improved by including different types of end sealing such as piston rings, O-rings to prevent air entrapment and reduce oil leakage from damper area. Current model uses Half-Sommerfeld boundary condition as cavitation modelling. As a future study, cavitation model can be improved by using different methods such as Gumbel or Elrod algorithm. Roughness of the surface can be included to the model to represent actual cases. Boundary conditions can be updated to simulate different oil supply lines to feed oil into damper clearance. A test set up where operating conditions are controlled precisely can be built to validate the numerical model. Improving the model with more realistic behavior of the system eliminates future test set-ups and give enough confident to rely on simulation results for different designs, lubricants, and operating conditions.

REFERENCES

[1] **Younan, A.A., Cao, J., Dimond, T.W. and Allaire, P.E.** (2011). Nonlinear analysis of squeeze film damper with entrained air in rotordynamic systems, *STLE J. Tribol.*, ***54(1)***, 132-144. doi:10.1080/10402004.2010.529543.

[2] **Tao, L., Diaz, S., Andrés, L.S. and Rajagopal, K.R**. (2000). Analysis of squeeze film dampers operating with bubbly lubricants, *ASME J. Tribol.,* ***122(1)***, 205-210. doi:10.1115/1.555344.

[3] **Xing, C., Horvat, F., Moldovan, S., Braun, M.J.** (2010). Experimental investigation of the development of cavitation in a squeeze film damper, *IJTC.,* ***41144***, 137-139. doi:10.1115/IJTC2010-41144.

[4] **Andrés, L.S.** (1987). Experimental measurement of the dynamic pressure distribution in a squeeze-film bearing damper executing circular-centered orbit, *ASME J. Tribol.*, ***30(3)***, 373-383. doi:10.1080/05698198708981770.

[5] **Andrés, L.S. and Jeung, S**. (2015). Experimental performance of an open ends, centrally grooved, squeeze film damper operating with large amplitude orbital motions, *ASME J. Eng. for Gas Turbines and Power*, ***137(3)***, 032508 (9 pages). doi:10.1115/1.4028376.

[6] **Delgado, A., and Andrés, L.S.** (2010). A model for improved prediction of force coefficients in grooved squeeze film dampers and oil seal rings, *ASME J. Tribol.*, ***132(3)***, 032202 (12 pages). doi:10.1115/1.4001459.

[7] **Andrés, L.S., Den, S., and Jeung, S.** (2018). On the force coefficients of a flooded, open ends short length squeeze film damper: from theory to practice (and back), *ASME Turbo Expo 2017: Turbomachinery Technical Conference and Exposition, GT2017-63152,* V07AT34A003; 12 pages.

[8] **Szeri, A.Z.** (1998). *Fluid Film Lubrication Theory & Design*, Cambridge, United Kingdom, The Press Syndicate of The University of Cambridge.

[9] **Andrés, L.A. and Vance, J.M.** (1987). Effects of fluid inertia on finite-length squeeze-film dampers, *ASME J. Tribol.*, ***30(3)***, 384-393. doi:10.1080/05698198708981771.

[10] **Hamzehlouia, S. and Behdinan, K.** (2017). A study of lubricant inertia effects for squeeze film dampers incorporated into high-speed turbomachinery, *Lubricants,* ***5 (4)***, 43. doi:10.3390/lubricants5040043.

[11] **Fan, T., Hamzehlouia, S., and Behdinan, K.** (2017). Experimental performance of an open ends, centrally grooved, squeeze film damper operating with large amplitude orbital motions, *JVE Journals*, ***19(8)***, 6122-6134. doi:10.1115/GT2014-25413.

[12] **Levesley, M.C., and Holmes, R**. (1996). The effect of oil supply and sealing arrangements on the performance of squeeze-film dampers: an experimental study, *SAGE Journals*, ***210(4)***, 221-232. doi:10.1243/PIME_PROC_1996_210_504_02.

[13] **Andrés, L.S., and Delgado, A**. (2007). Identification of force coefficients in a squeeze film damper with a mechanical end seal—part I: unidirectional load tests, *ASME J. Eng. for Gas Turbines and Power*, ***129(3)***, 858-864. doi: 10.1115/1.2436571.

[14] **Mu. C., Darling, J., and Burrows, C.R.** (1991). An appraisal of a proposed active squeeze film damper, *ASME J. Tribol.*, ***113(4)***, 750-754. doi: doi.org/10.1115/1.2920688.

[15] **Cusano, C. and Funk, P.E.** (1977). Transmissibility study of a flexibly mounted rolling element bearing in a porous bearing squeeze-film damper, *ASME J. Tribol.*, ***99(1)***, 50-56. doi:10.1115/1.3452989.

[16] **Khonsari, M.M. and Booser, E.R.** (2008). *Applied Tribology: Bearing Design and Lubrication*, John Wiley & Sons, Ltd.

[17] **Andrés, L.S. and Delgado, A.** (2008). Squeeze film damper with a mechanical end seal: experimental force coefficients derived from circular centered orbits, *ASME J. Eng. for Gas Turbines and Power*, ***130(4)***, 042505/1-8. doi:10.1115/1.2800345.

[18] **Jeung, S., Andrés, L.S., Den, S. and Koo, B.** (2019). Effect of oil supply pressure on the force coefficients of a squeeze film damper sealed with piston rings, *ASME J. Tribol.*, ***141(6)***, 061701/1-11. doi:/10.1115/1.4043238.

CURRICULUM VITAE

Name Surname	**: Ekin Akbulut**
Place and Date of Birth	**: Altındağ/Ankara, 7 October 1992**
E-Mail	**: ekinakbulut@ymail.com**

EDUCATION	**:**
B.Sc.	**:** 2010, Hacettepe University, Engineering Faculty, Mechanical Engineering Automotive Engineering Programme

PROFESSIONAL EXPERIENCE:

- 2015-present(2020) : General Electric Aviation – Mechanical Design Engineer
    - Aeroderivative engine bearings and sump hardware design and analysis